Supporting Information for "Global geomagnetic field evolution from 900 to 700 ka including the Matuyama-Brunhes reversal"

Ahmed Nasser Mahgoub [1,2], Monika Korte [1], and Sanja Panovska[1]

[1]Helmholtz Centre Potsdam GFZ German Research Centre for Geosciences, Section 2.3 – Geomagnetism, Potsdam, Germany. [2]Geology Department, Assiut University, Assiut, 71516, Egypt.

Contents of this file

This supplementary material contains eight sections with mainly figures illustrating the following topics discussed in the main manuscript:

1. Regularization, data rejection and misfit statistics.
2. Model predictions compared to input sediment records.
3. Model predictions compared to lava data.
4. Time-averaged field during MB reversal.
5. Kamikatsura excursion (∼890–884 ka)

Corresponding author: Ahmed Nasser Mahgoub, `ahmedn@gfz-potsdam.de`

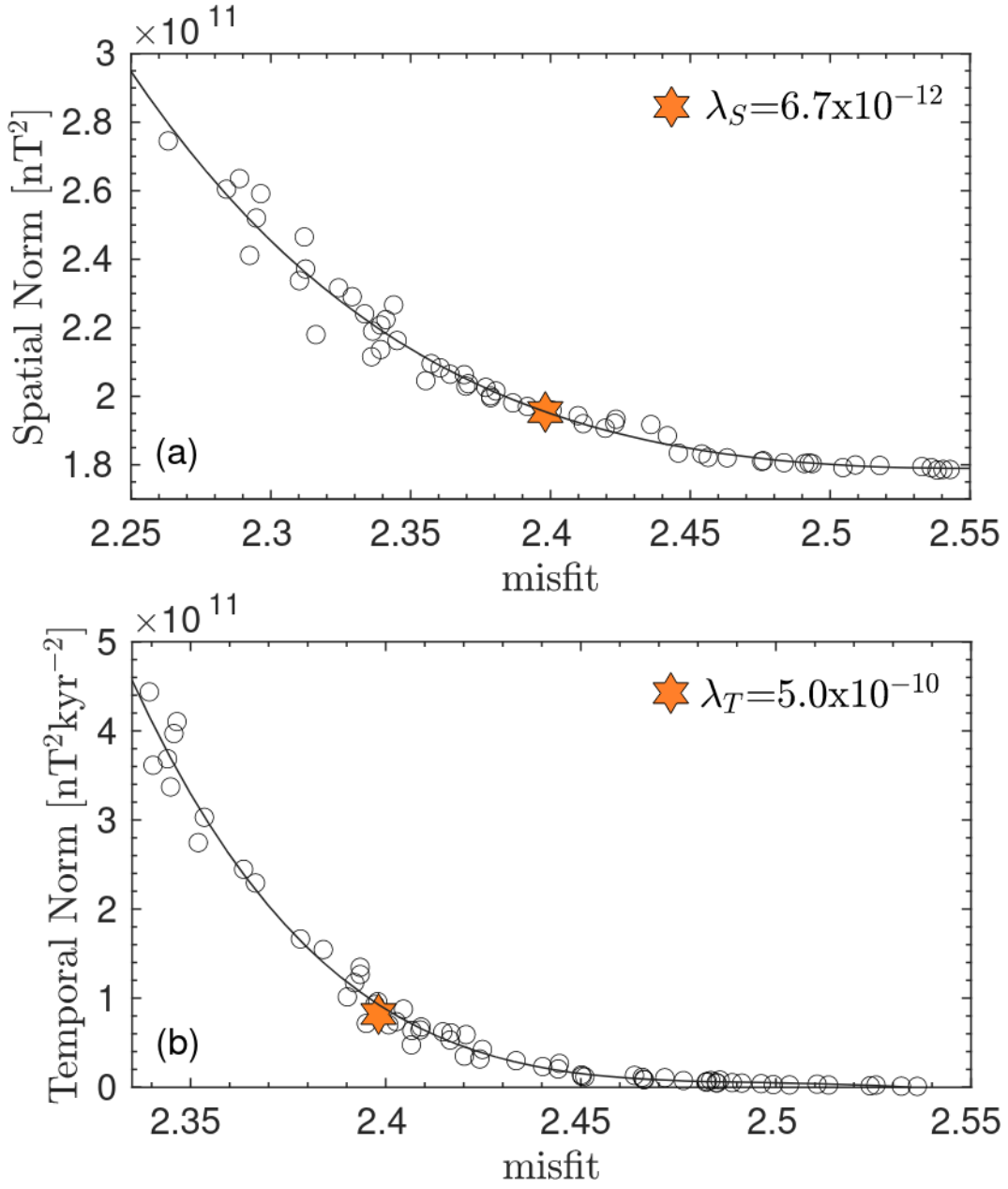## S1 Regularization, data rejection and misfit statistics

Figure S1: Trade-off between spatial (top) and temporal (bottom) model complexity against misfit between model and data depending on the spatial λ_S and temporal λ_T regularization factors (circles). Our preferred λ_S and λ_T parameters (stars) are located at the knees of the L-curves and take the values $\lambda_S = 6.7 \times 10^{-12}$; and $\lambda_T = 5.0 \times 10^{-10}$.
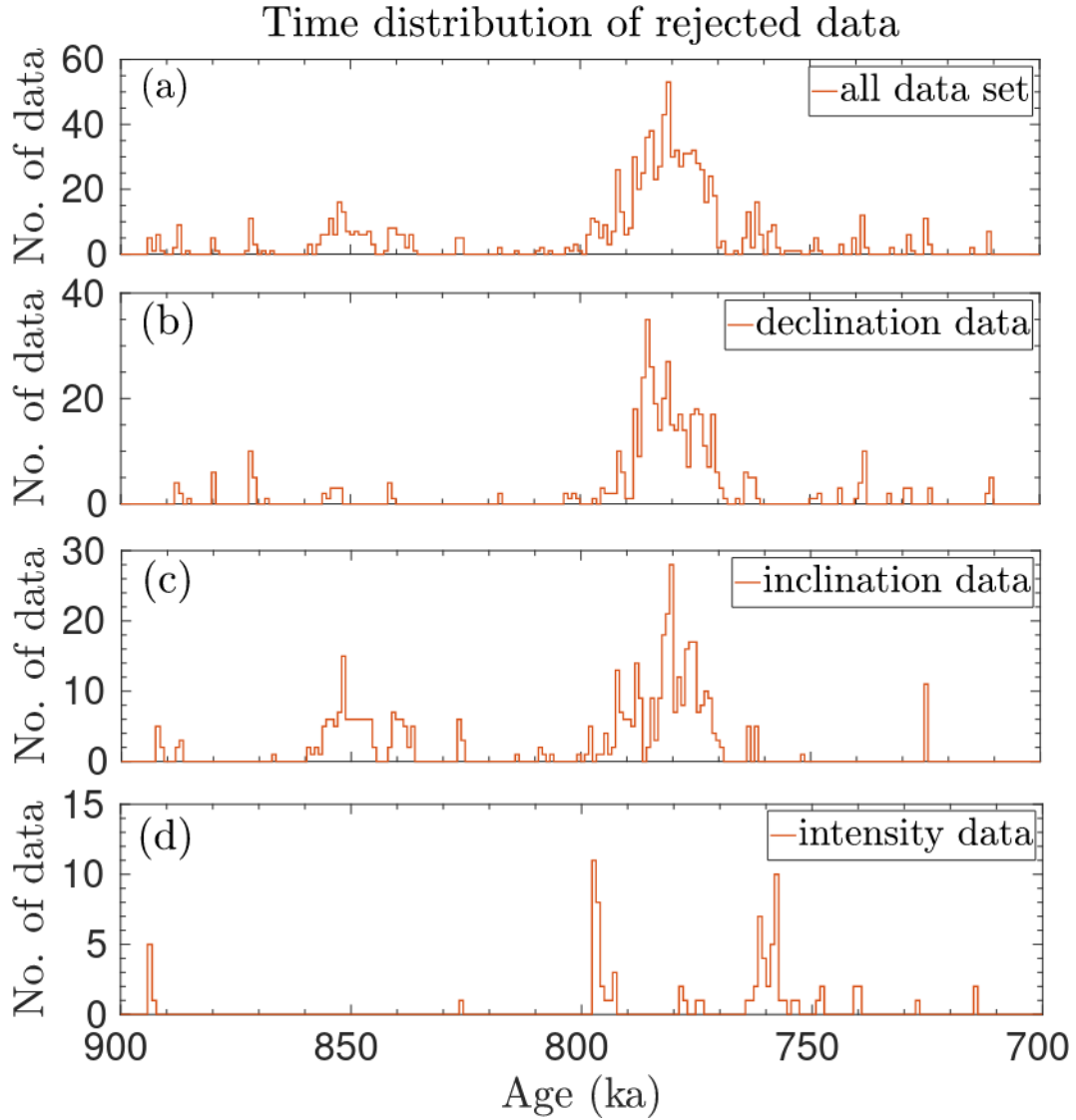
Figure S2: Temporal distributions of all magnetic field component data (a), and separately of declination (b), inclination (c), and intensity (d) that were rejected during the GGFMB model construction. Rejection was done by iterative rejection at 10 standard deviations. The data are binned in 1000 years intervals.
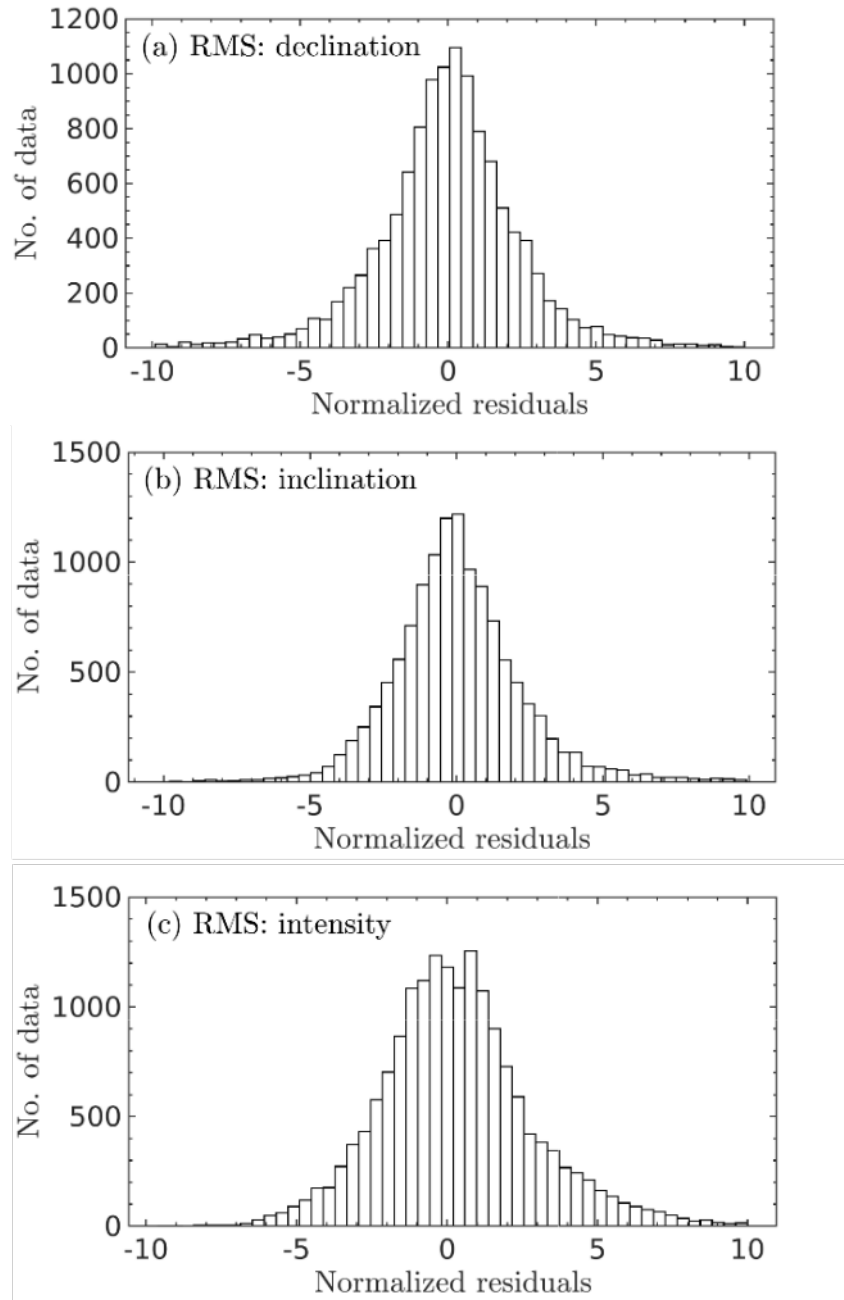
Figure S3: Distribution of RMS misfits of declination (a), inclination (b), and intensity (c). The RMS values are normalized by the data uncertainty estimates.

S2 Model predictions compared to input sediment records

Predictions from the GGFMB model are compared to the 38 input data series (figures S4-S41). There are 17 records with full vector field data, 5 have two field components, and the remaining 16 have only one magnetic field component.

In each graph, declination, inclination, and intensity data are represented by black circles and the GGFMB model prediction is represented by a red line. Prediction from the earlier IMMAB4 model of Leonhardt and Fabian (2007) are included for comparison as a light blue line.
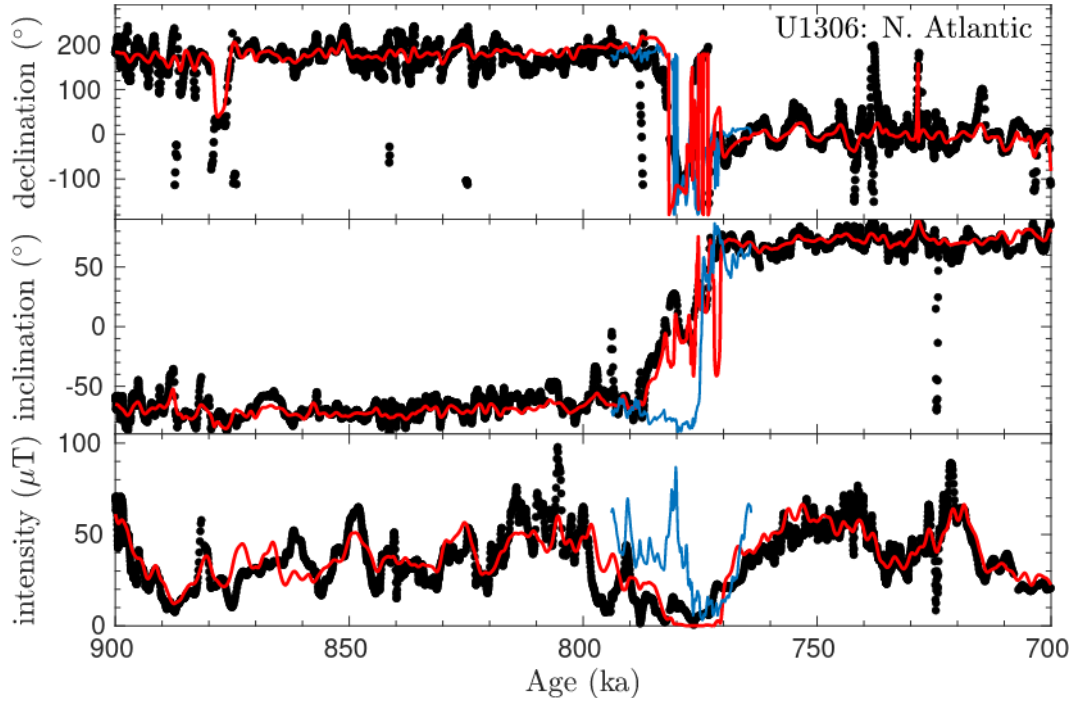
Figure S4: GGFMB model prediction for North Atlantic record (U1306)
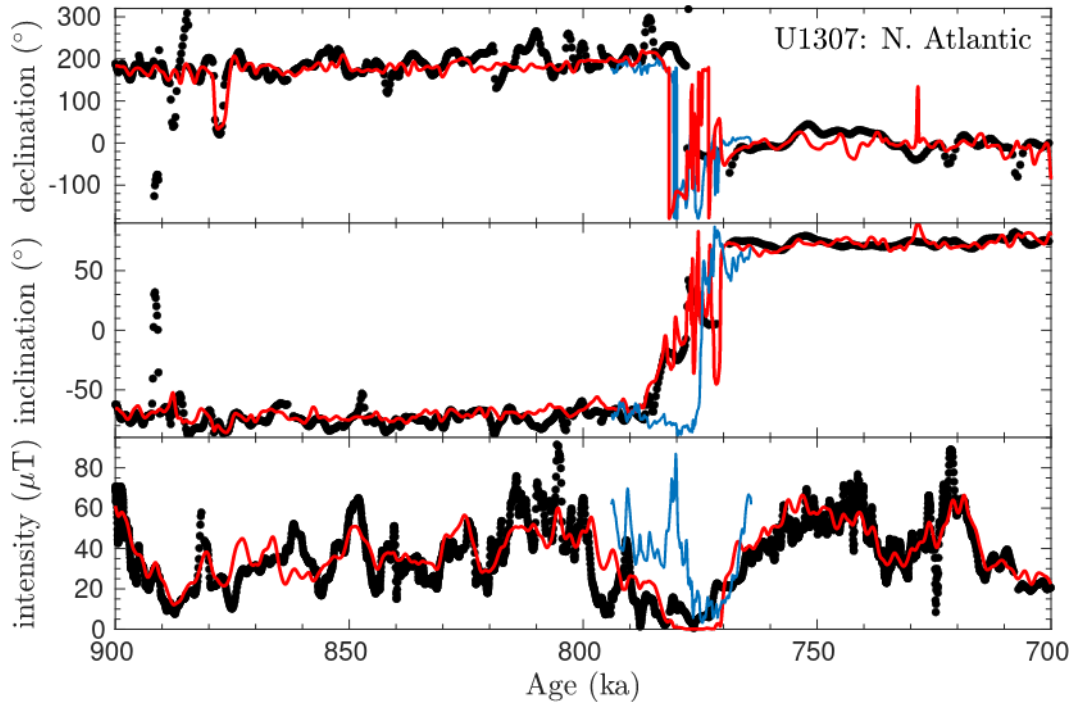
Figure S5: GGFMB model prediction for North Atlantic record (U1307)
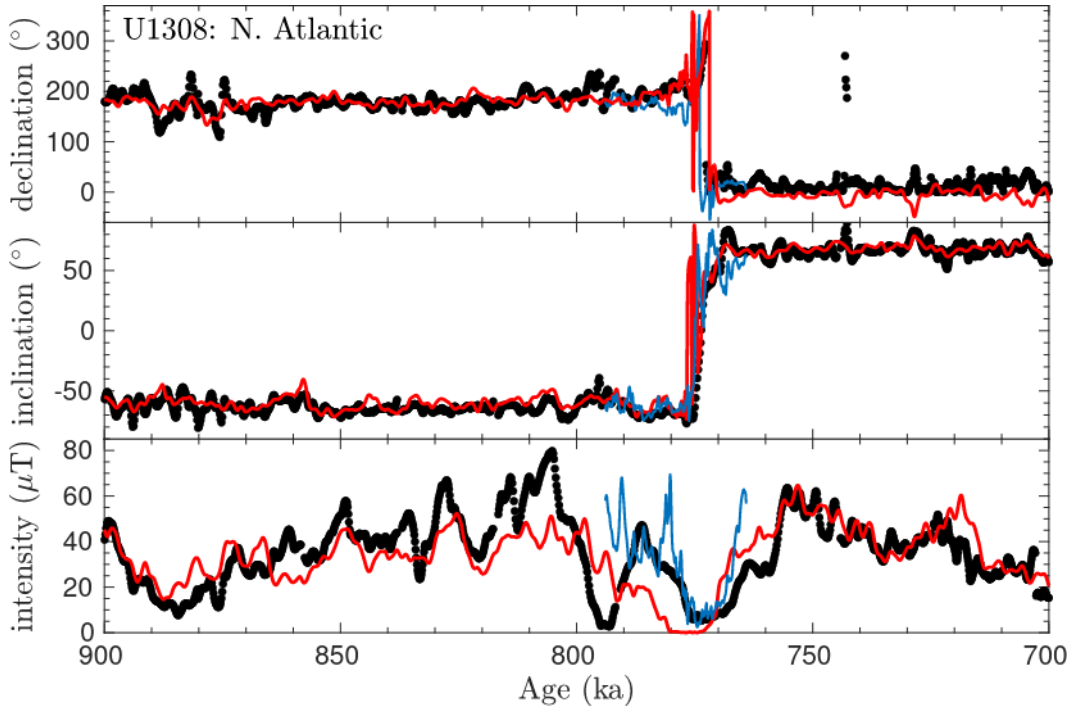
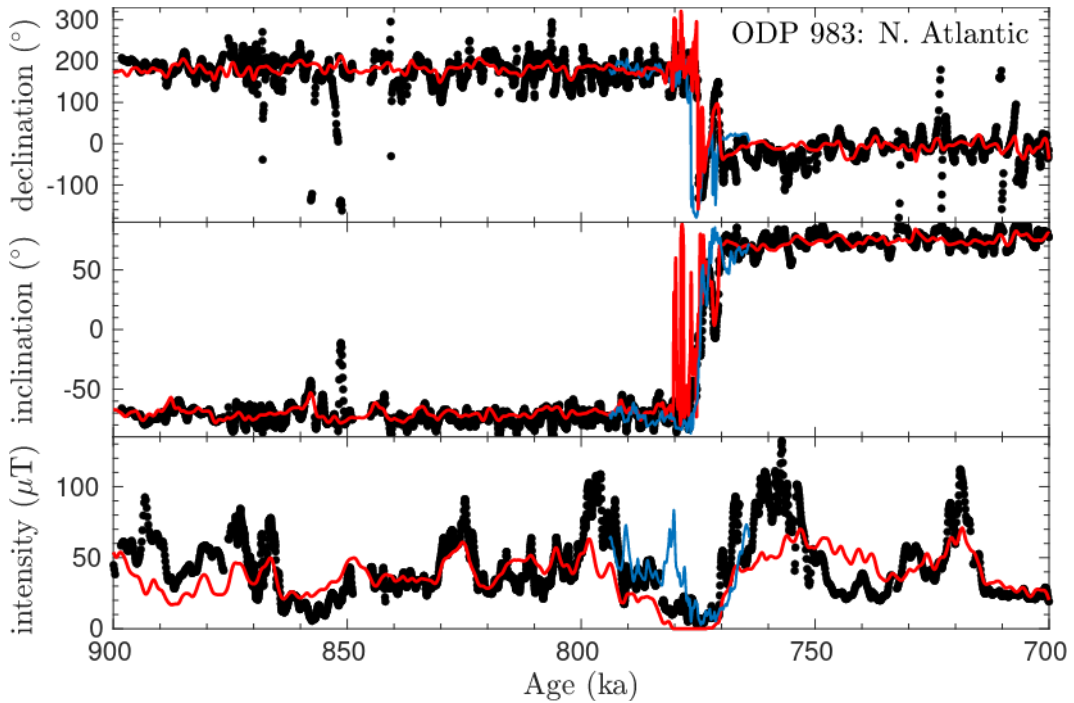Figure S6: GGFMB model prediction for North Atlantic record (U1308).

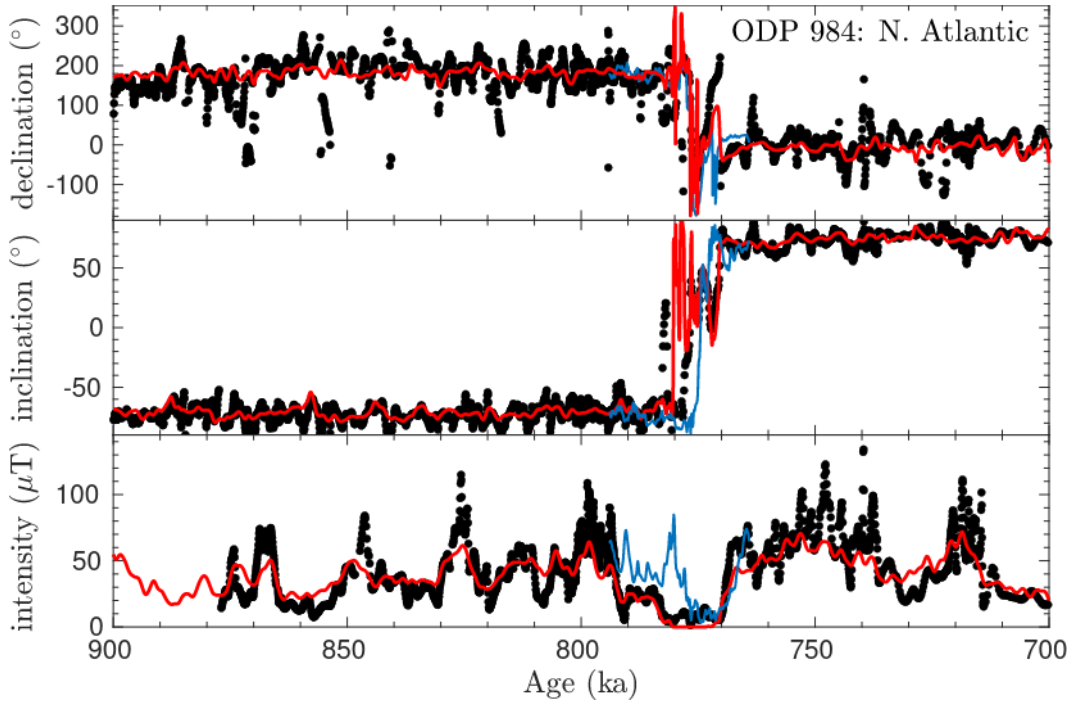Figure S7: GGFMB model prediction for North Atlantic record (ODP 983)

Figure S8: GGFMB model prediction for North Atlantic record (ODP 984)
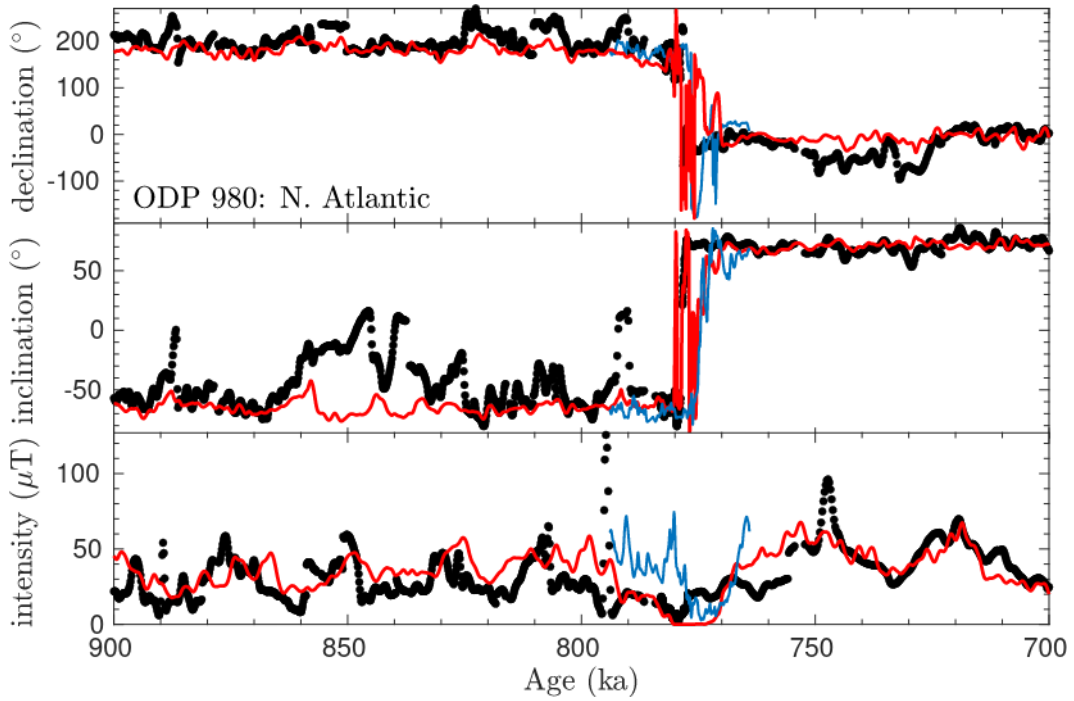

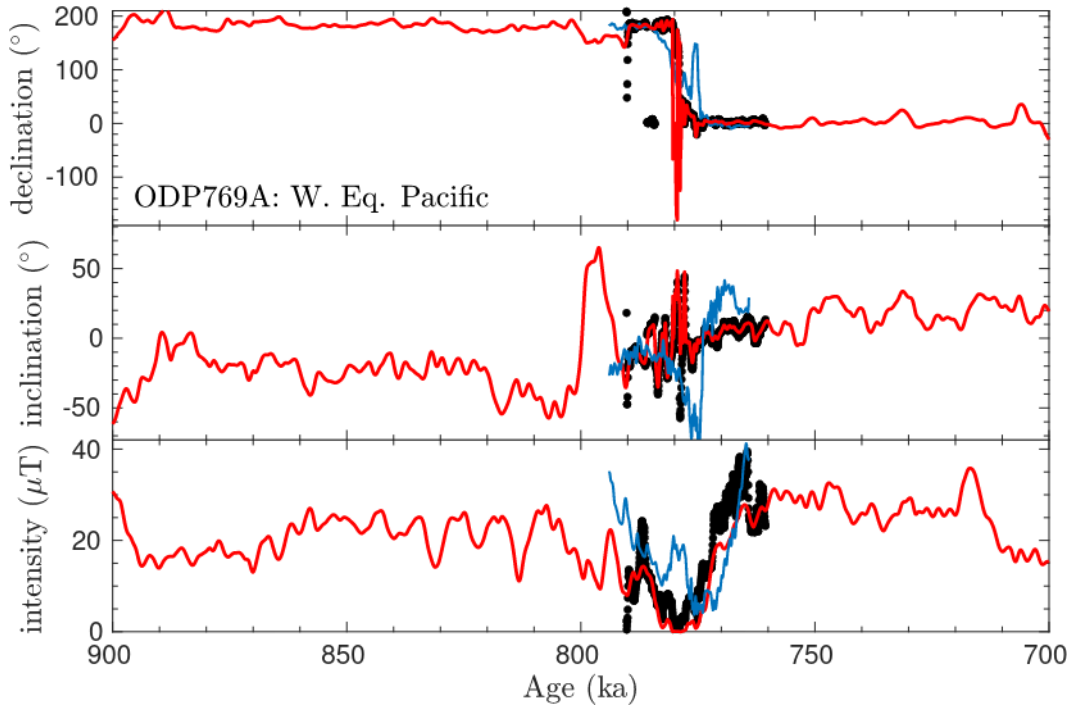Figure S9: GGFMB model prediction for North Atlantic record (ODP 980)

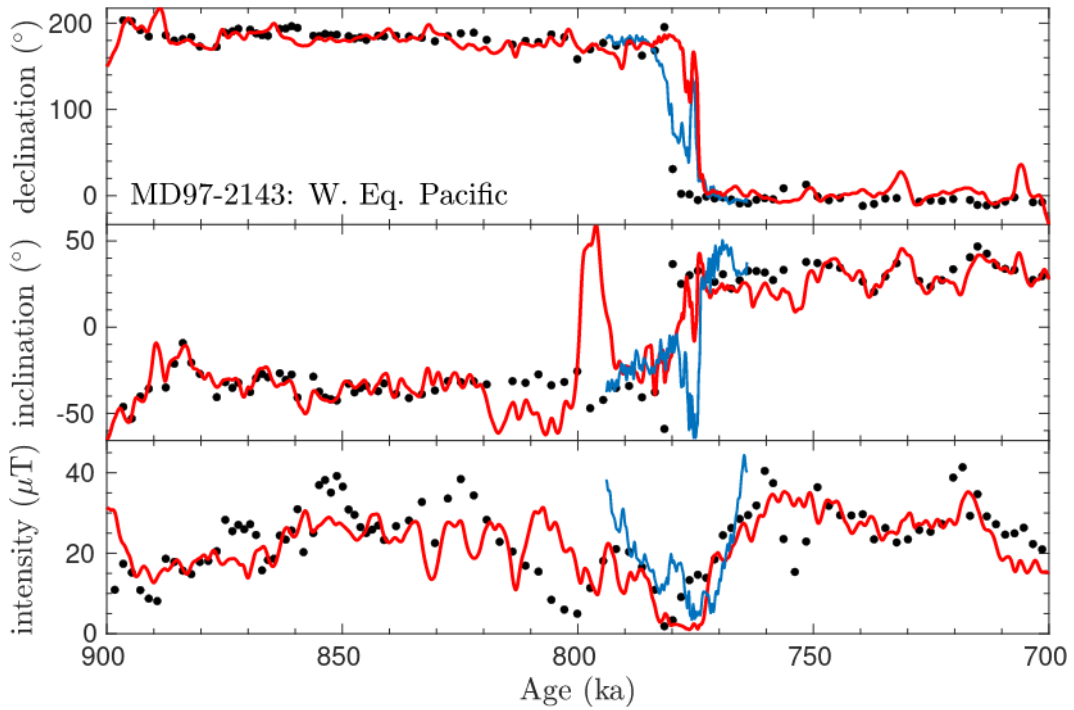Figure S10: GGFMB model prediction for Western Equatorial Pacific record (ODP 769A).

Figure S11: GGFMB model prediction for Western Equatorial Pacific record (MD97-2143).
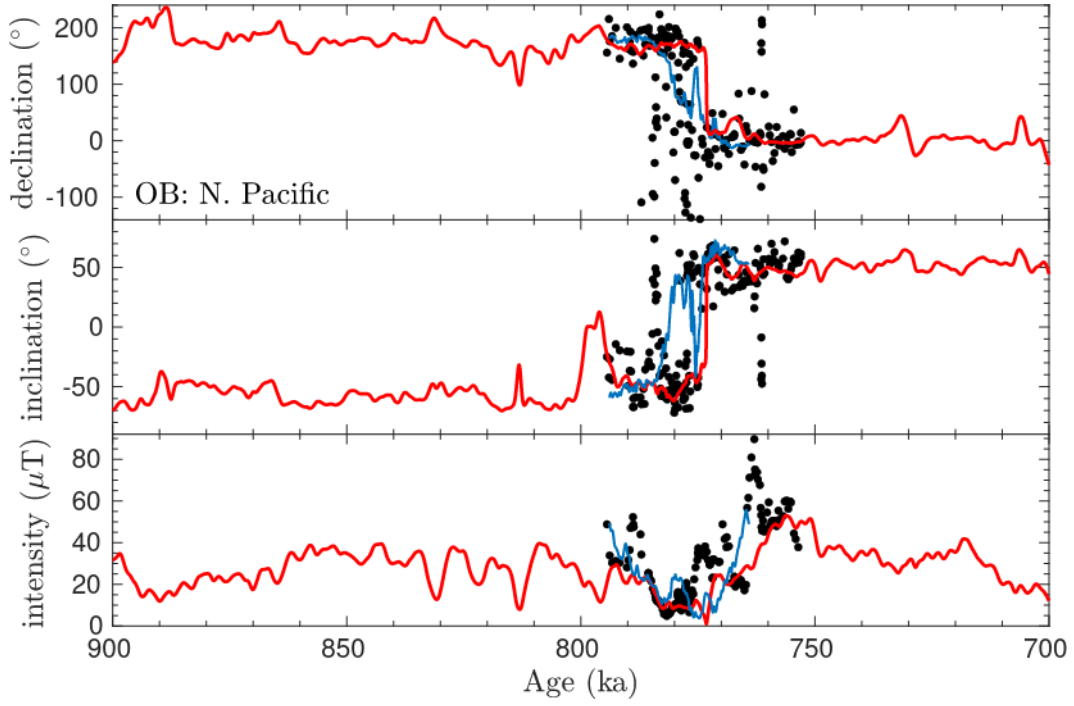
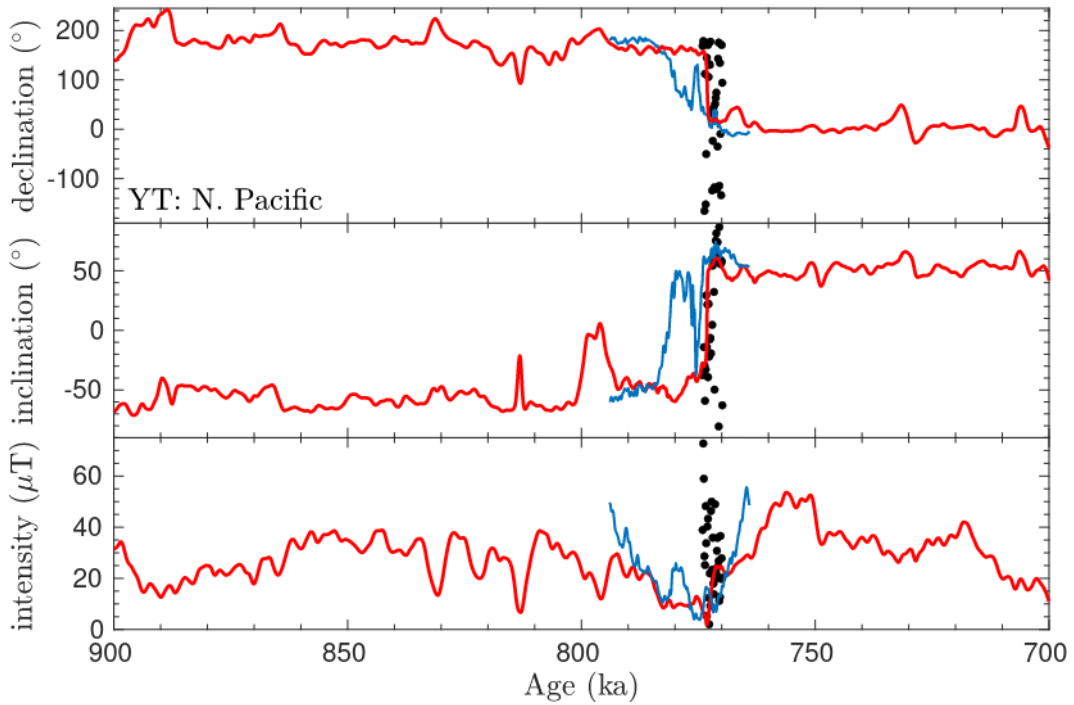Figure S12: GGFMB model prediction for North Pacific record (OB).

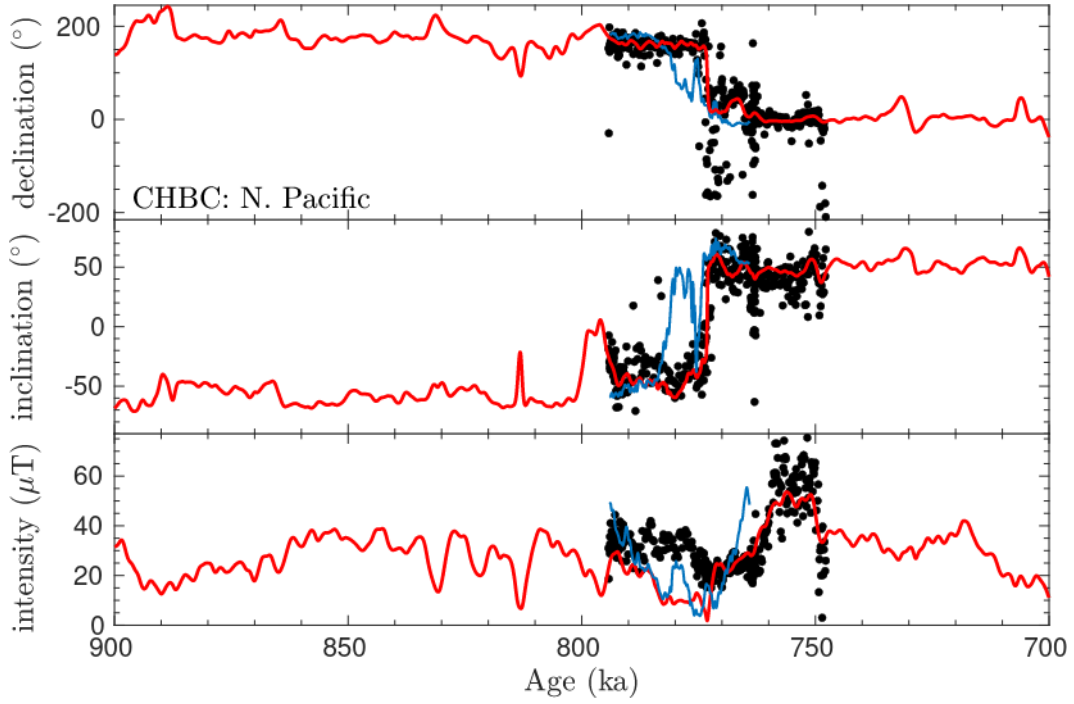Figure S13: GGFMB model prediction for North Pacific record (YT).

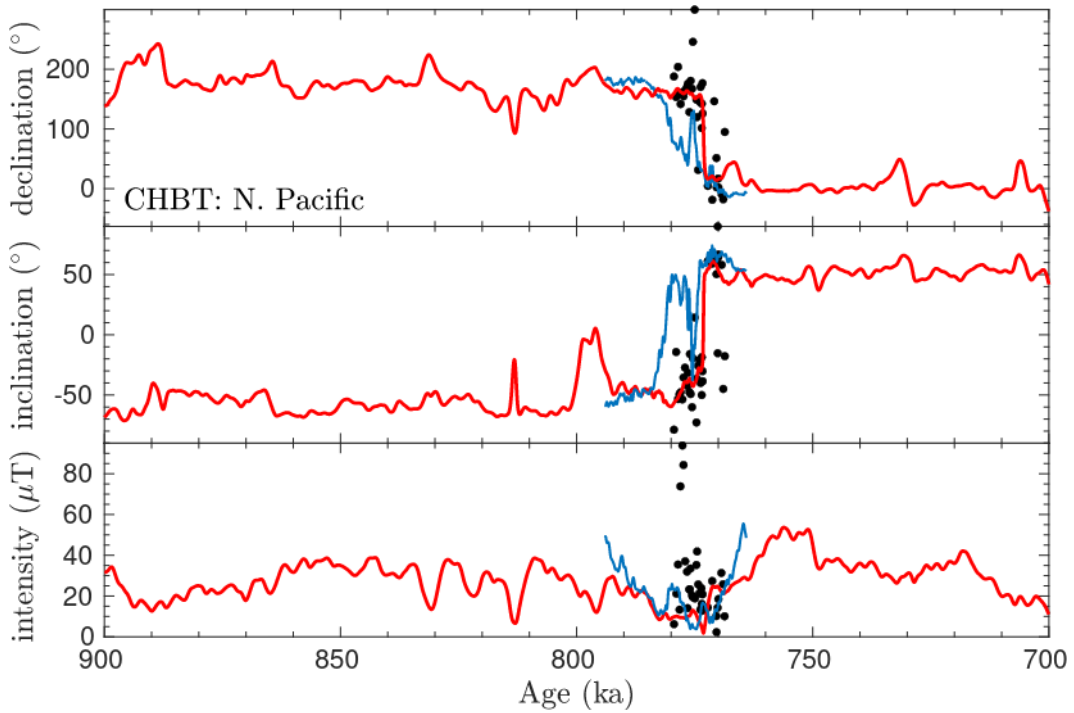Figure S14: GGFMB model prediction for North Pacific record (CHBC).

Figure S15: GGFMB model prediction for North Pacific record (CHBT).
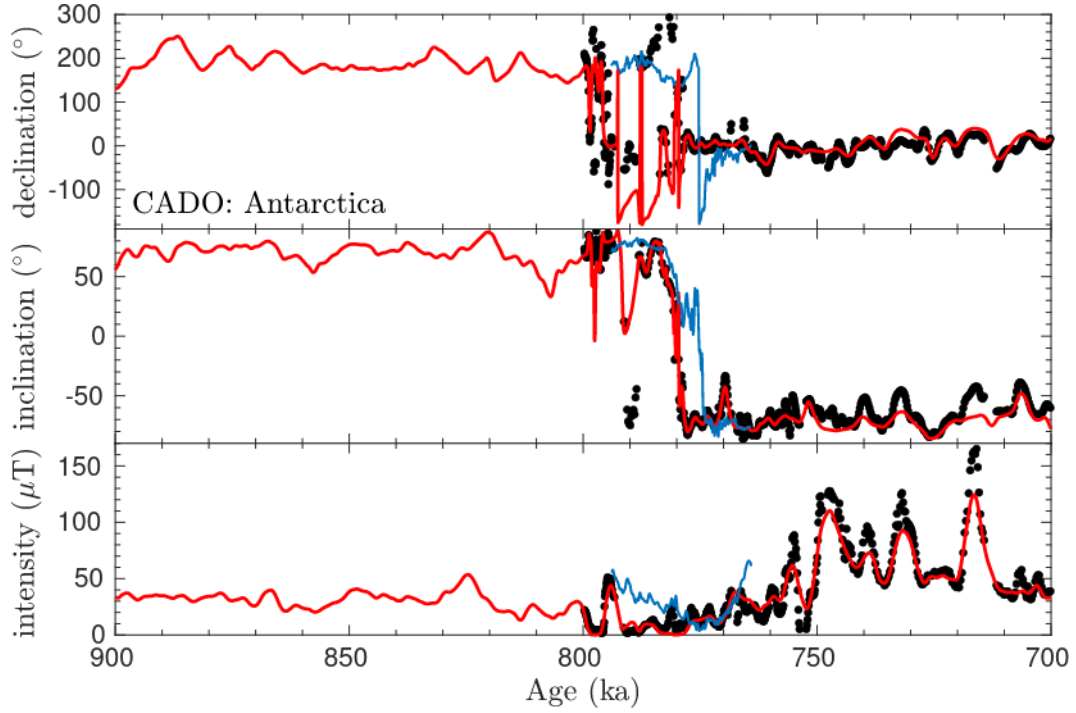
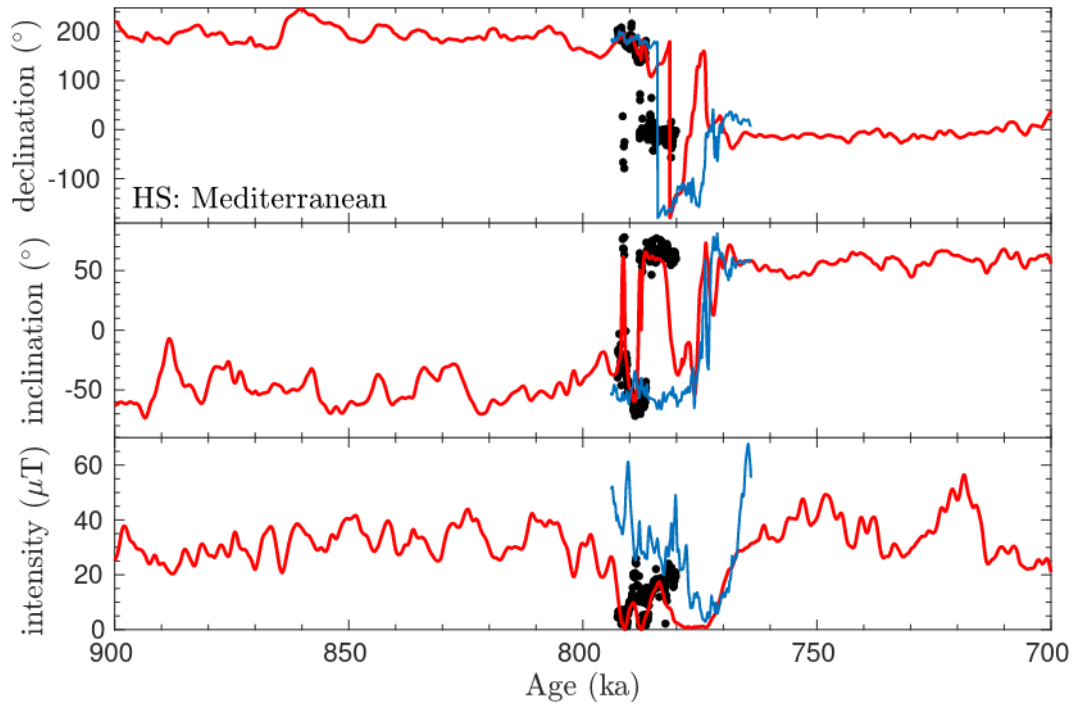Figure S16: GGFMB model prediction for Antarctica record (CADO).

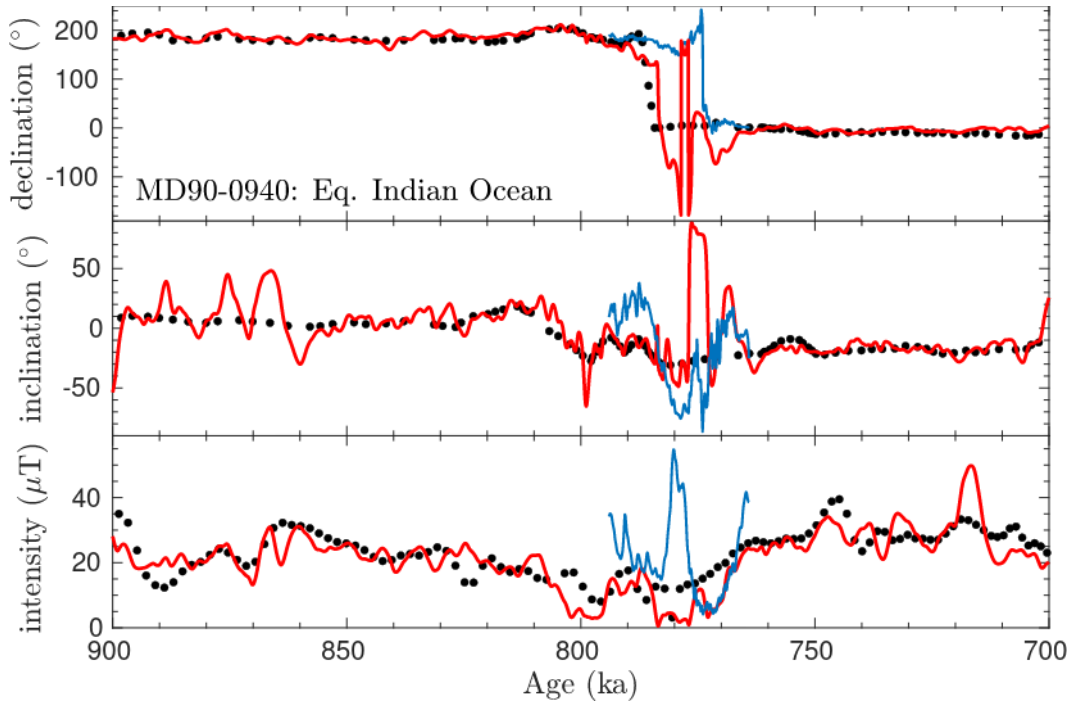Figure S17: GGFMB model prediction for Mediterranean record (HS).

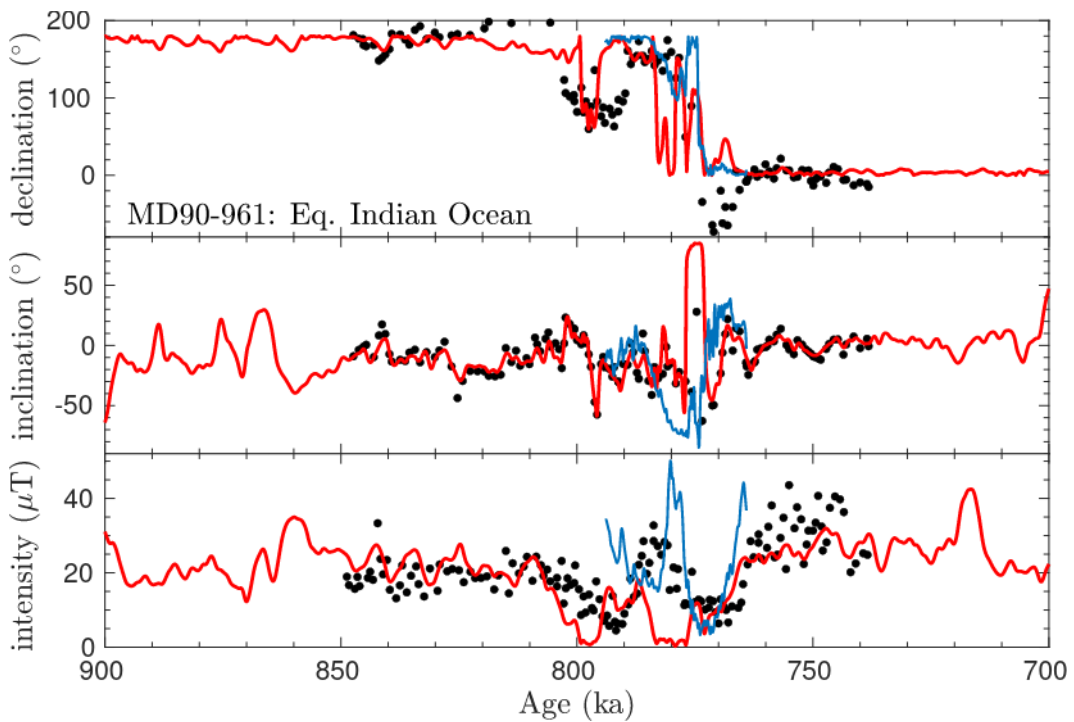Figure S18: GGFMB model prediction for Equatorial Indian Ocean record (MD90-0940).

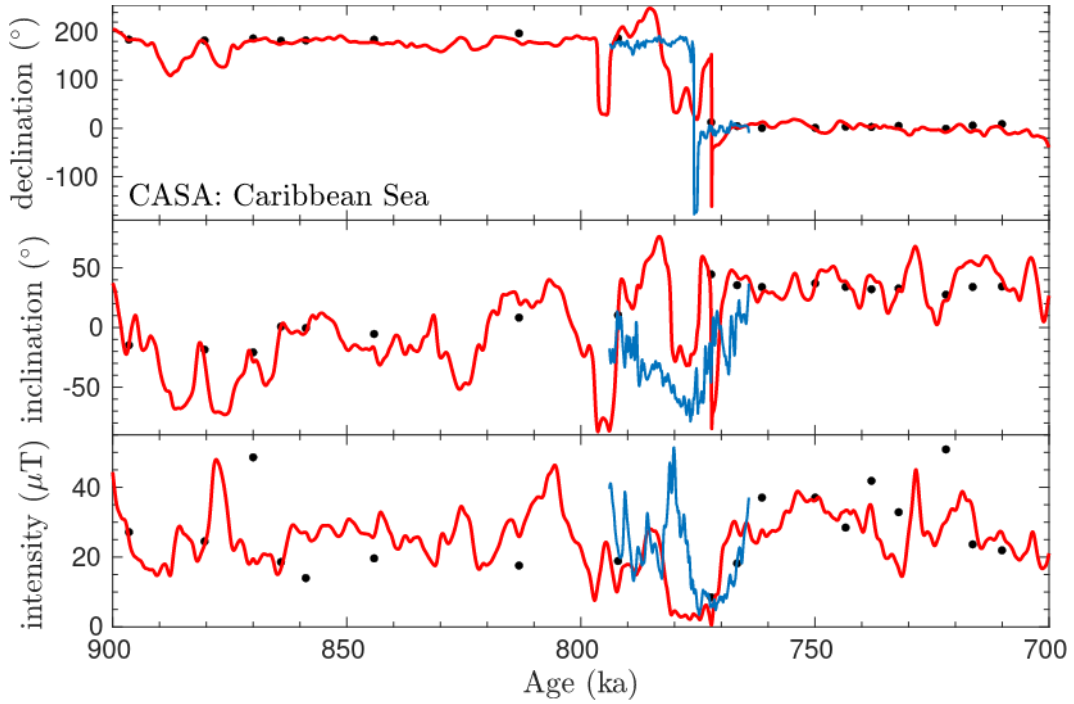Figure S19: GGFMB model prediction for Equatorial Indian Ocean record (MD90-961).

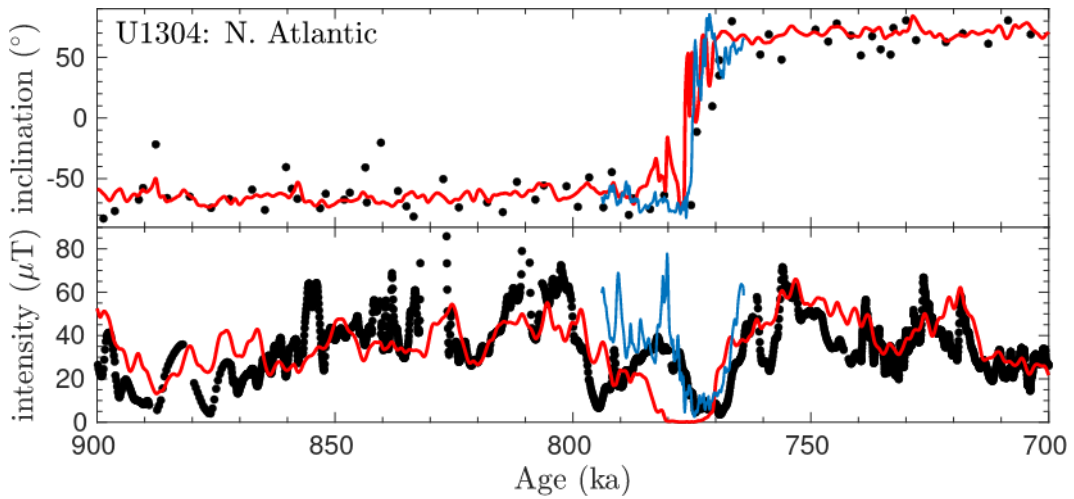Figure S20: GGFMB model prediction for Caribbean Sea record (CASA).

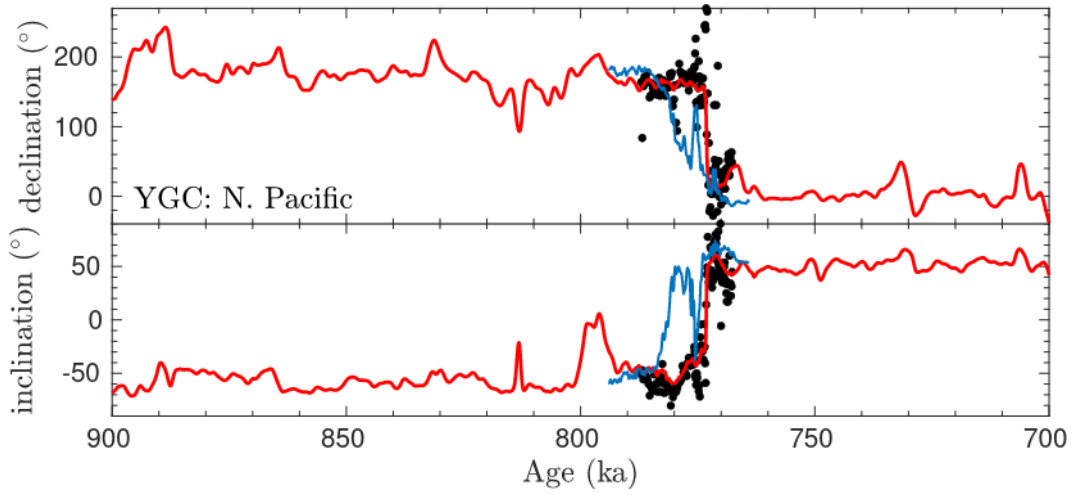Figure S21: GGFMB model prediction for North Atlantic record (U1304)

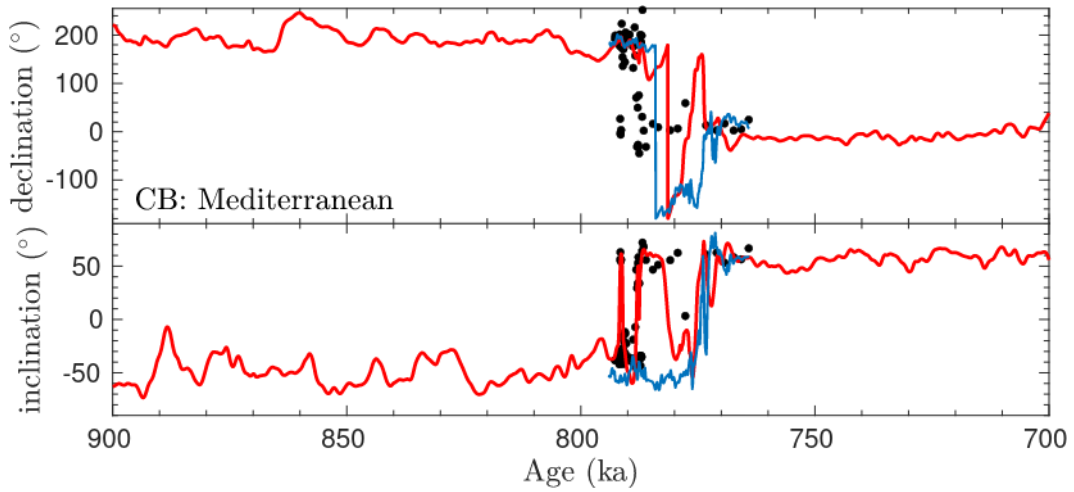Figure S22: GGFMB model prediction for North Pacific record (YGC).

Figure S23: GGFMB model prediction for Mediterranean record (CB).
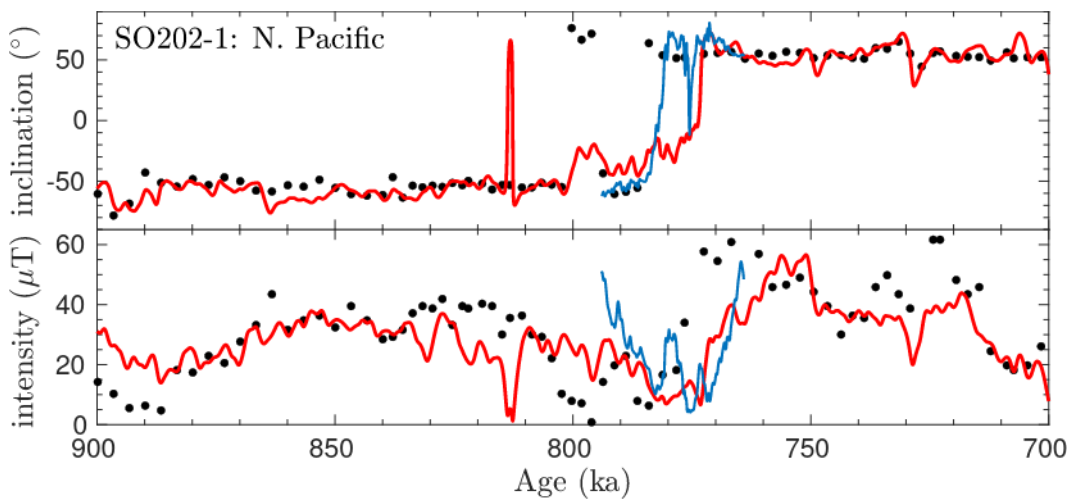

Figure S24: GGFMB model prediction for North Pacific record (SO202-1).
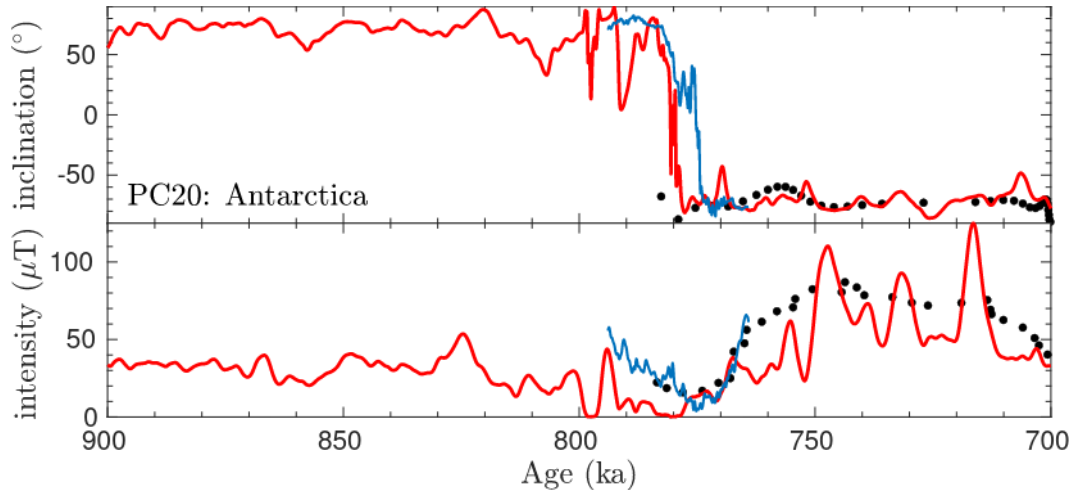
Figure S25: GGFMB model prediction for Antarctica record (PC20).

Figure S26: GGFMB model prediction for Russian Arctic record (ICDP-5011).
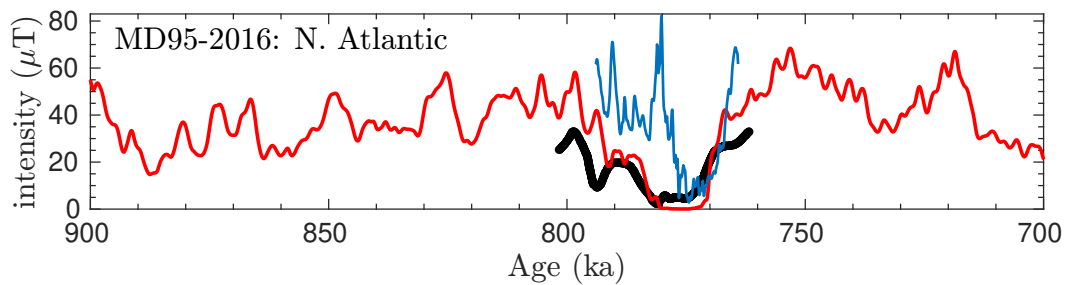
Figure S27: GGFMB model prediction for North Atlantic record (MD95-2016).

Figure S28: GGFMB model prediction for Western Equatorial Pacific record (KH73-4-7).

Figure S29: GGFMB model prediction for Western Equatorial Pacific record (KH73-4-8).

Figure S30: GGFMB model prediction for Western Equatorial Pacific record (KH90-3-5).

Figure S31: GGFMB model prediction for Western Equatorial Pacific record (MD98-2183).

Figure S32: GGFMB model prediction for Western Equatorial Pacific record (MD98-2185).
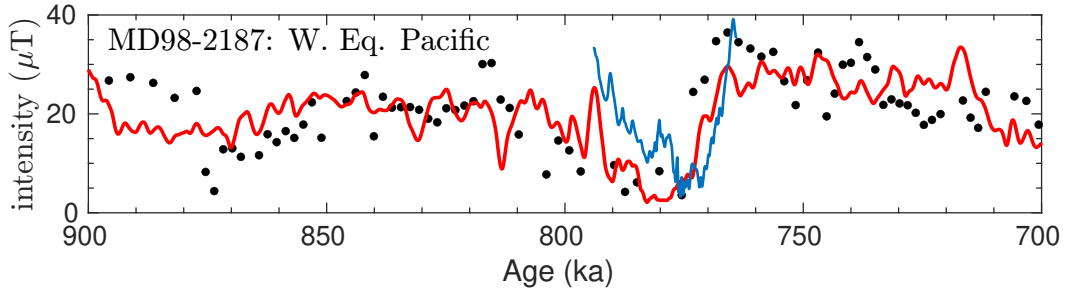
Figure S33: GGFMB model prediction for Western Equatorial Pacific record (MD98-2187).
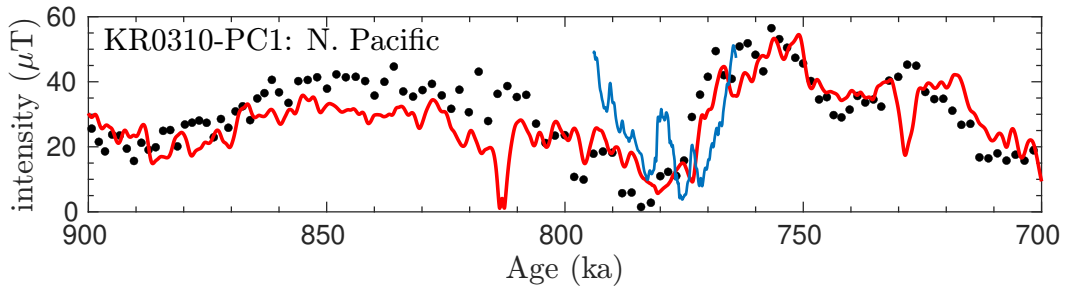
Figure S34: GGFMB model prediction for North Pacific record (KR0310-PC1).
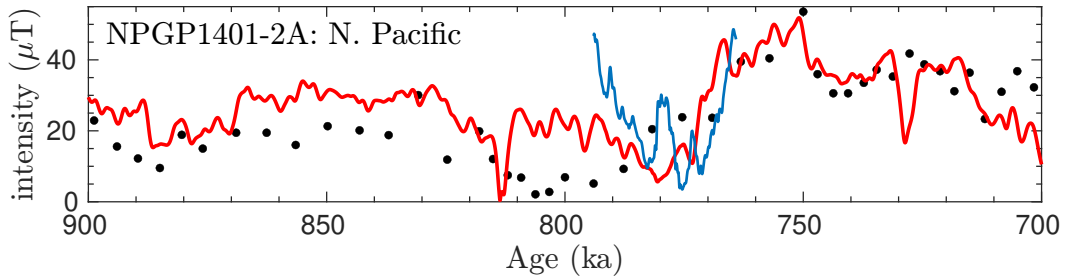
Figure S35: GGFMB model prediction for North Pacific record (NPGP1401-2A).
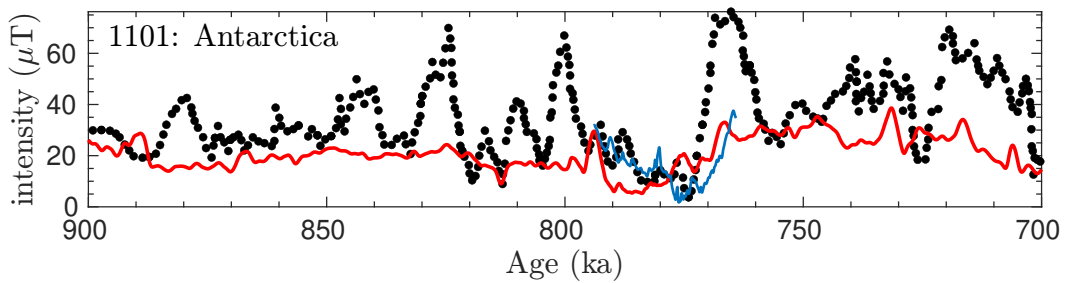
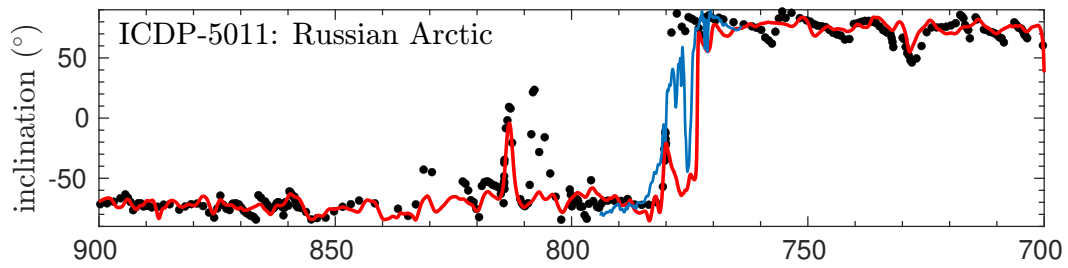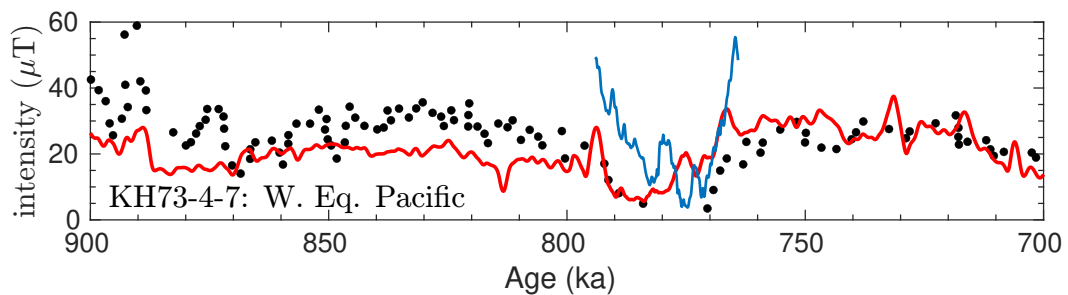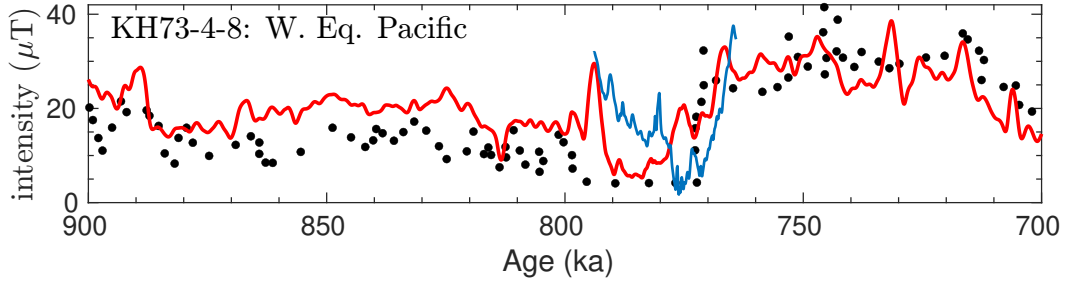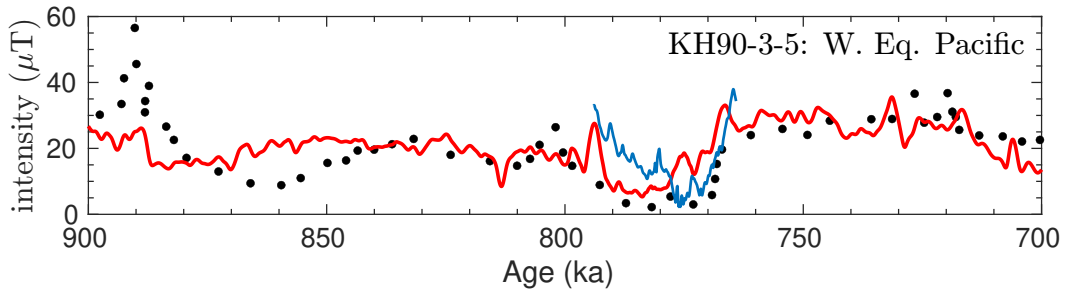Figure S36: GGFMB model prediction for Antarctica record (1101).
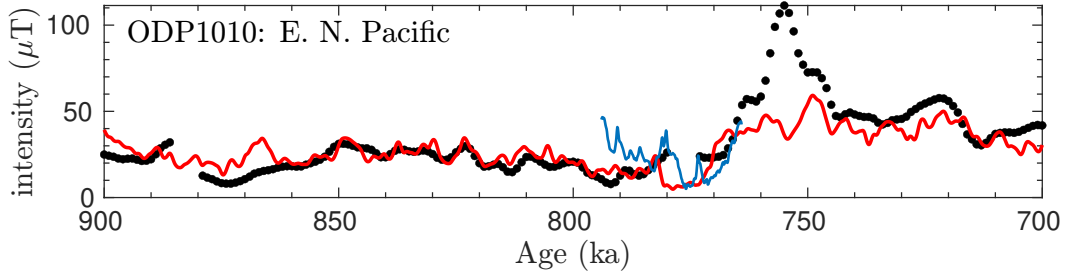
Figure S37: GGFMB model prediction for Eastern Northern Pacific record (ODP 1010).
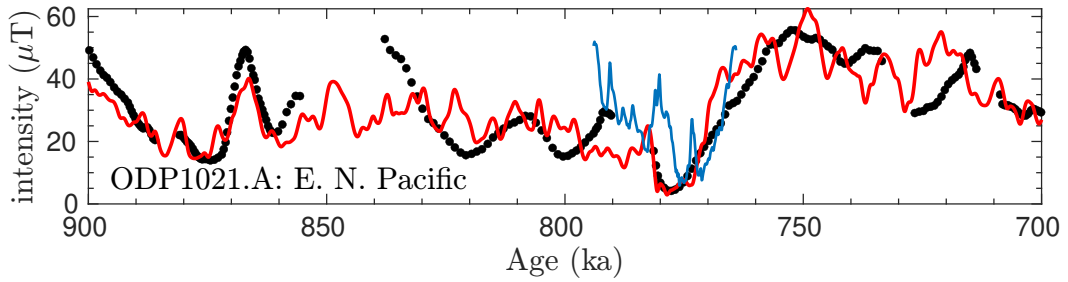
Figure S38: GGFMB model prediction for Eastern Northern Pacific record (ODP 1021.A).

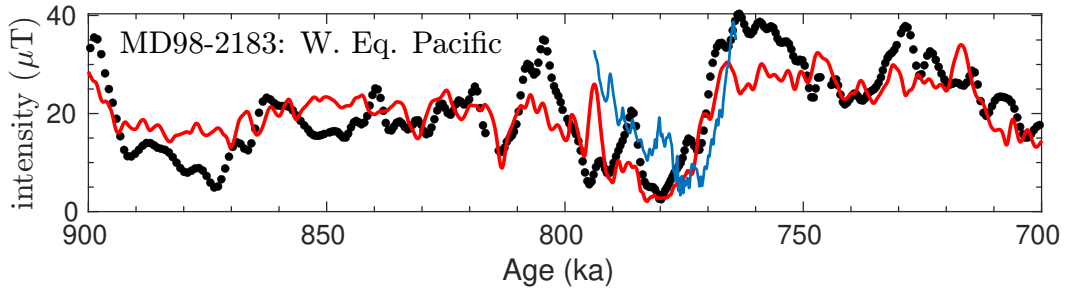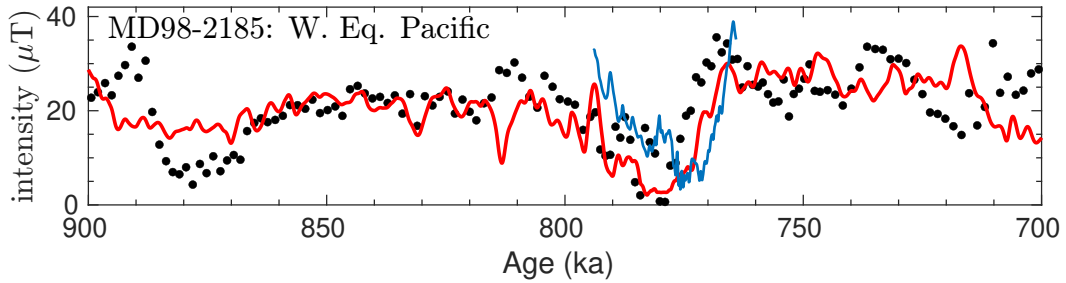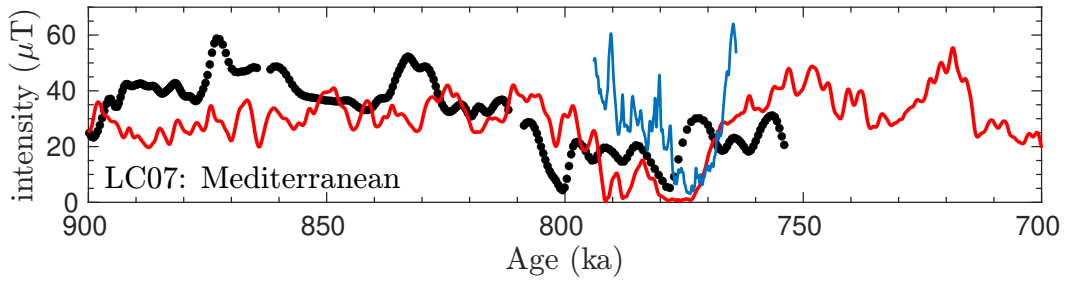Figure S39: GGFMB model prediction for Mediterranean record (LC07).
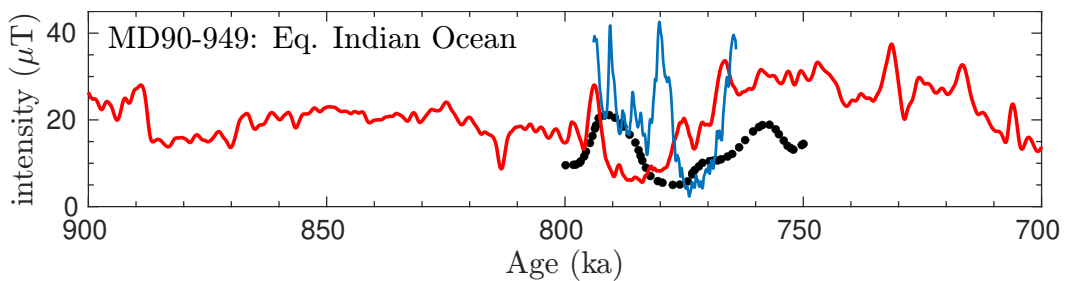
Figure S40: GGFMB model prediction for Equatorial Indian Ocean record (MD90-949).
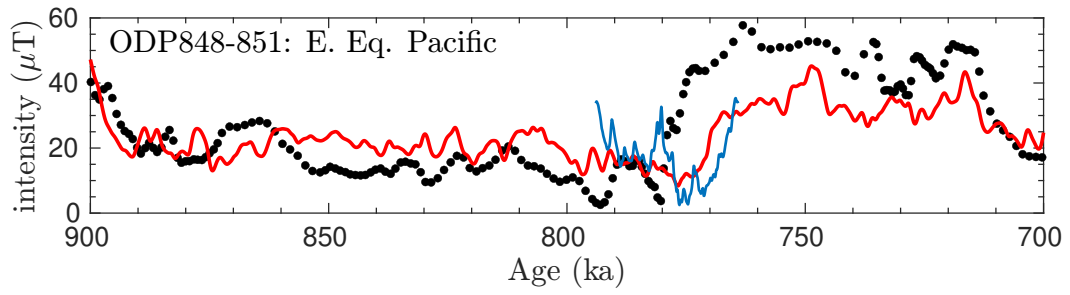
Figure S41: GGFMB model prediction for Eastern Equatorial Pacific record (ODP 848-851).

S3 Model predictions compared to lava data

GGFMB model predictions are compared to independent thermal remanent magnetization (TRM) data from lavas, that have not been used to derive the model. The lava data come from 11 regions and have been re-located by dipole assumption to a central location, for which the model prediction has been calculated. Prediction of GGFMB to 9 lava regions are shown in figures S42–S50. The paleomagnetic data of lavas are represented by black dots, the model predictions by red lines. Predictions from IMMAB4 model are also shown by light blues lines for comparison.
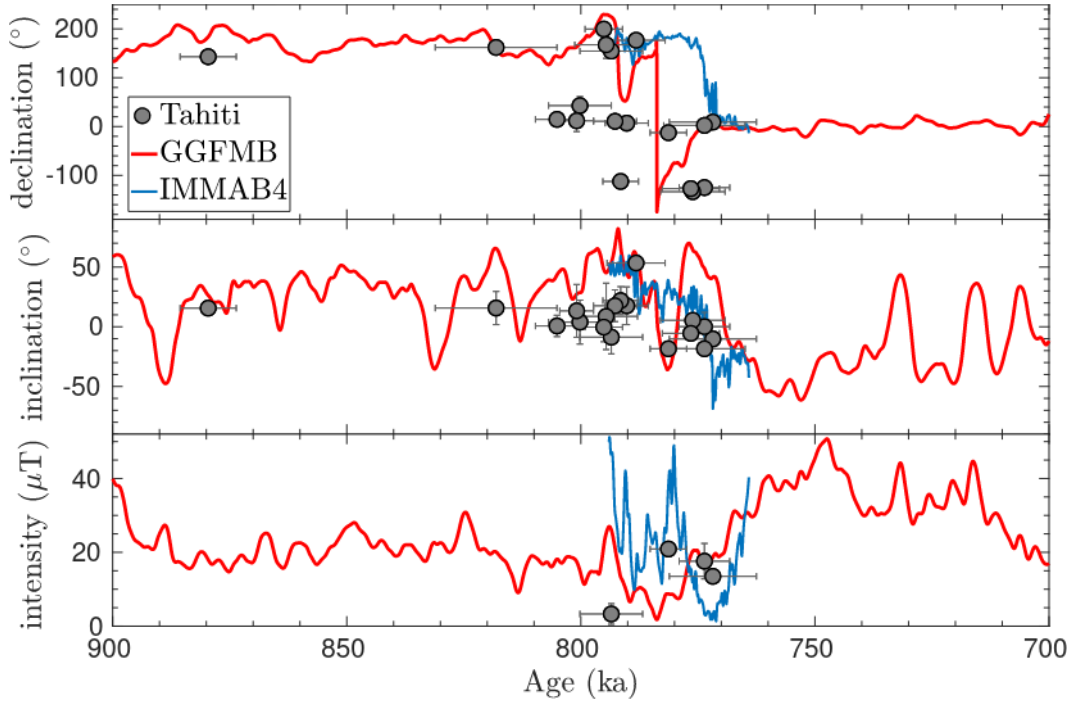
Figure S42: GGFMB model prediction for Tahiti lavas data.
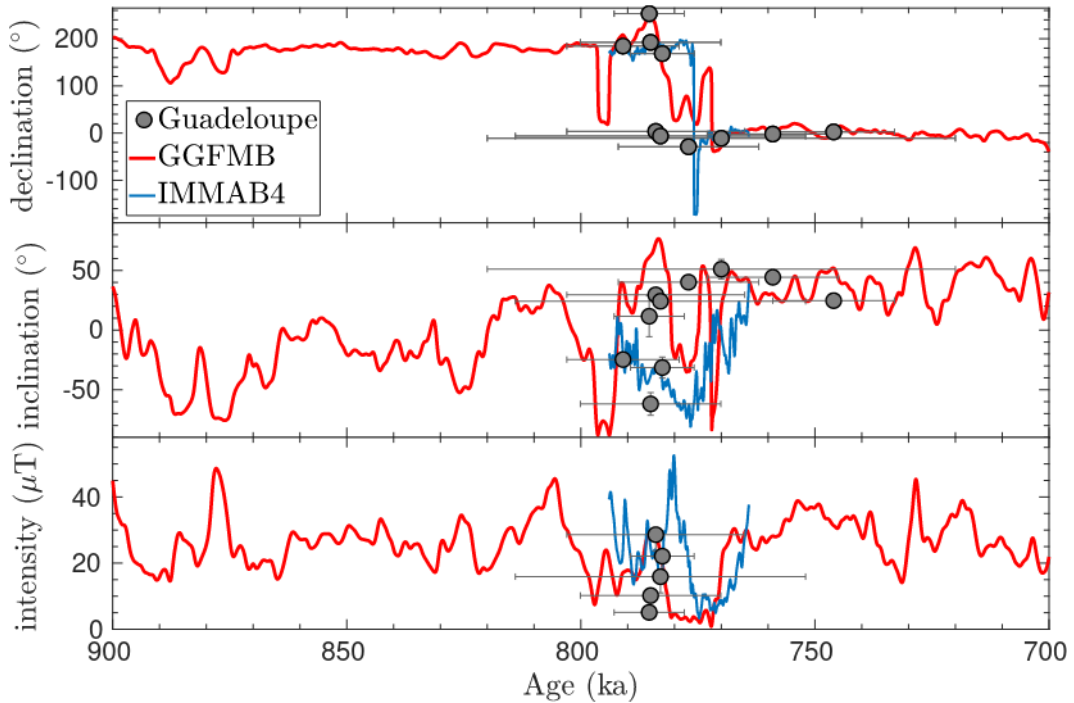
Figure S43: GGFMB model prediction for Guadeloupe lavas data.
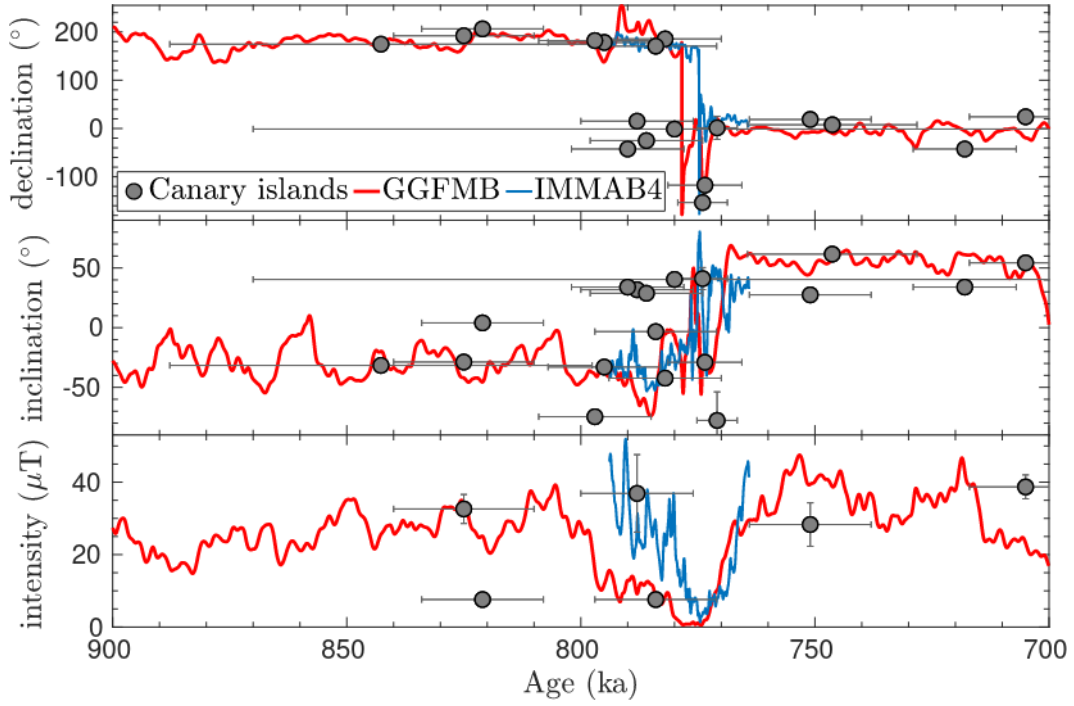
Figure S44: GGFMB model prediction for Canary islands lavas data.
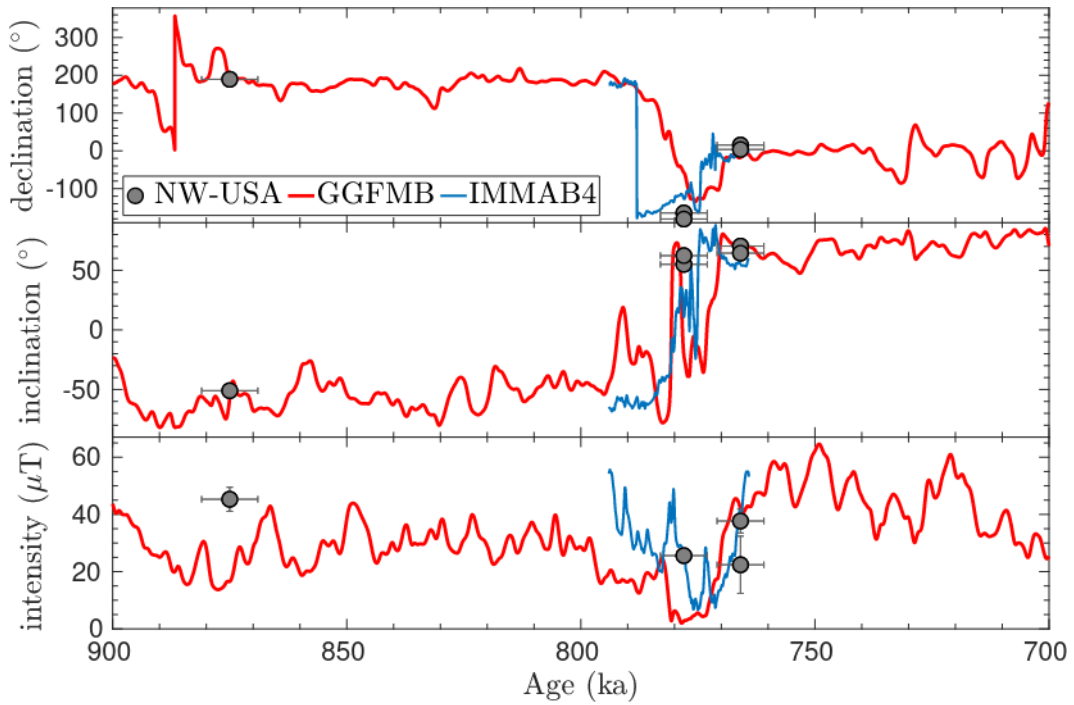
Figure S45: GGFMB model prediction for NW-USA lavas data.
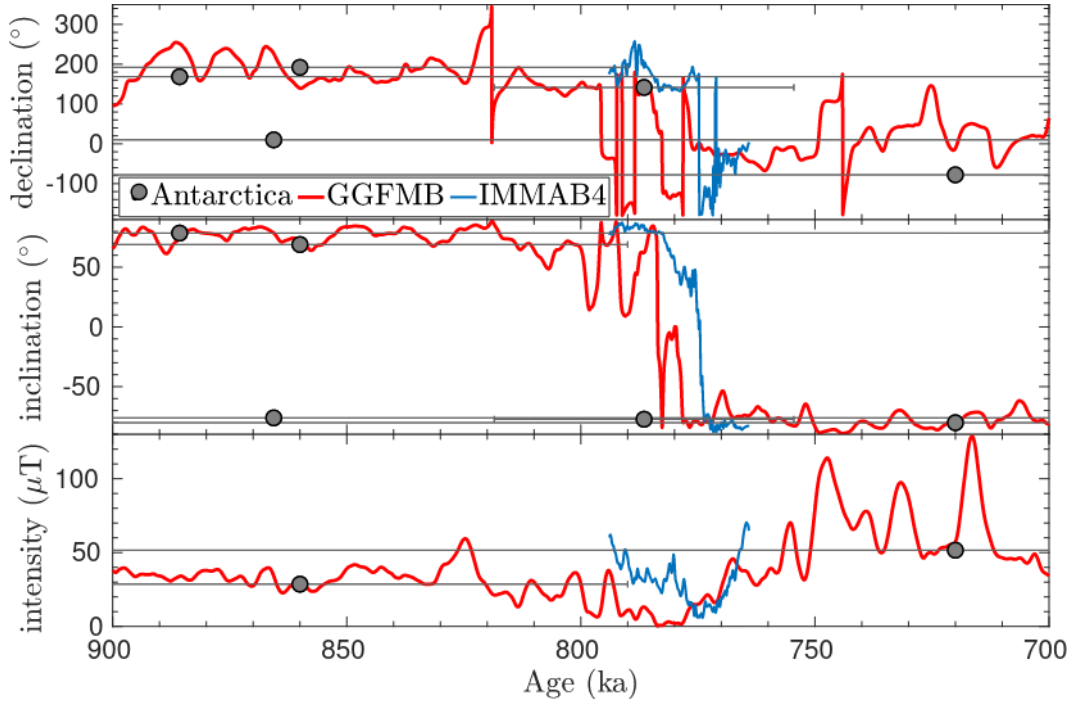
Figure S46: GGFMB model prediction for lavas data from Antarctica.
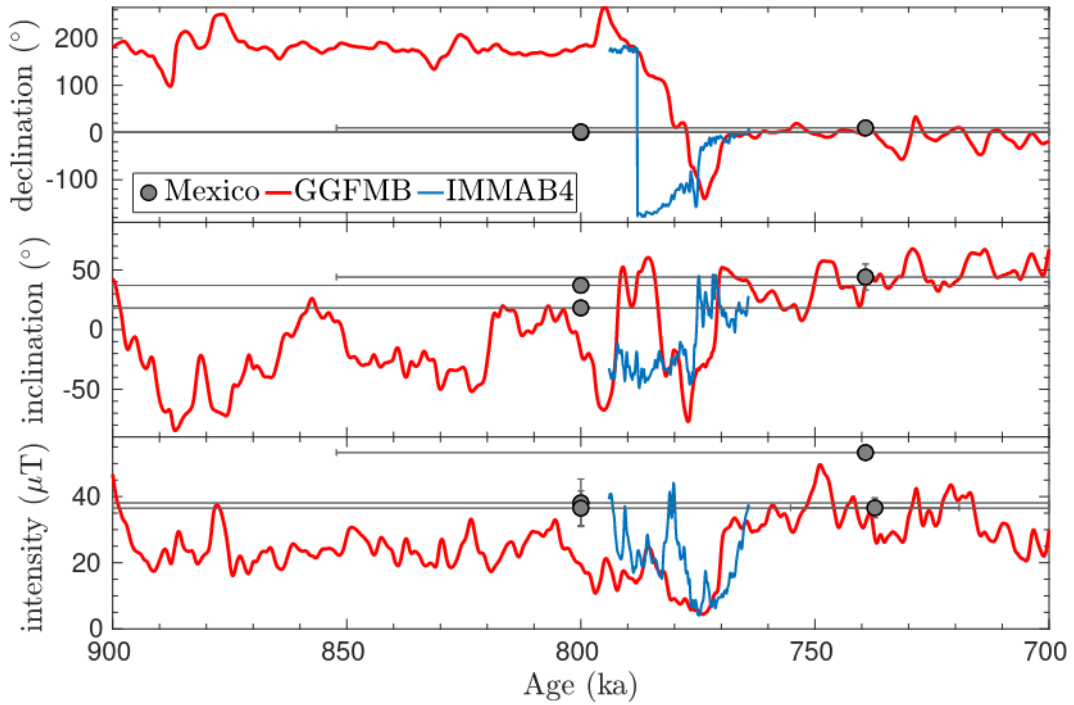
Figure S47: GGFMB model prediction for lavas data from Mexico.
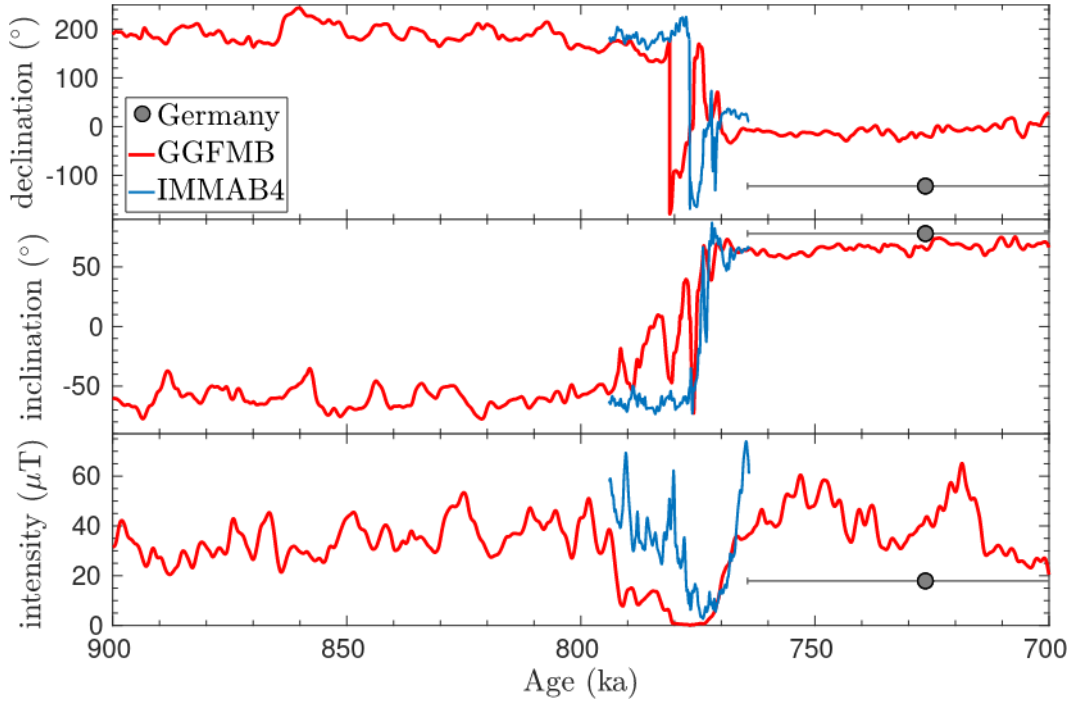
Figure S48: GGFMB model prediction for lavas data from Germany.
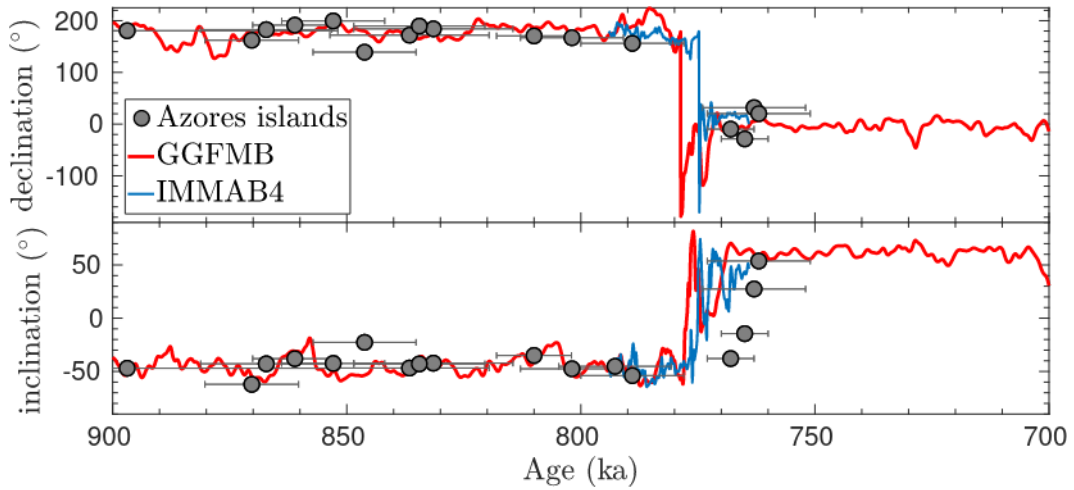
Figure S49: GGFMB model prediction for Azores islands lavas data.
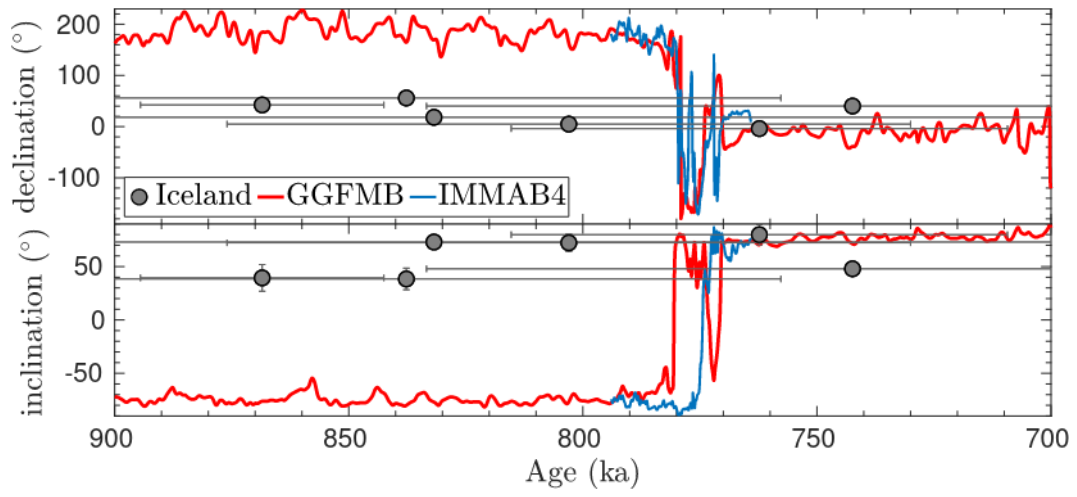
Figure S50: GGFMB model prediction for Iceland lavas data.

³² **S4 Time-averaged field during MB reversal**

MB reversal (799-770 ka)

IMMAB4 (794-764 ka)

IT08 (801-769 ka)

(a) F at Earth's surface **(b) Br at CMB** **(c) Br NAD at CMB**

Figure S51: Time-averaged field during the MB reversal, calculated from GGFMB model (this study), IMMAB4 (Leonhardt & Fabian, 2007), and IT08 (Ingham & Turner, 2008). The calculated components are: intensity (F) at the Earth's surface (b); radial field (B_r) at the CMB; and non-axial dipole (NAD) of the B_r at the CMB. Note that maps of B_r and NAD of B_r are on different scale.

S5 Kamikatsura excursion ($\sim$ 890–884 ka)

Paleomagnetic data of lava flows and sediment records of age period 900–860 ka are investigated here. Over this time period, virtual dipole moment (VDM) and virtual geomagnetic pole (VGP) latitude data were recorded from 6 lava locations (Tahiti, Hawaii, Iceland, Azores Islands, NW-USA, and Antarctica) and 12 sediment records (U1306, U1307, U1308, ODP983, ODP984, ODP980, MD97-2143, MS90-0940, MD90-961, CAS16-24PC, U1304, and SO202-1). Records U1304 and SO202-1 have inclination and intensity data while the rest 10 record have full vector data (See Table 1). Mahgoub et al. (2023) provides details on ages, paleomagnetic directions, and paleointensities of these sediment records and lavas.

The geographical locations of the lavas are depicted in Fig. S52a, VDM and VGP of the lavas and sediment records are plotted in Fig. S52b–c. Moreover, the paleosecular variation index (P_i) of the sediment records is plotted in Fig. S52d. Also, the DM, DL, and P_i estimated from GGFMB are plotted (Fig. S52a–d). From Fig. S52, it can be seen that between 890 and 884 ka records U1306, U1307, U1304, U1308, ODP984, and ODP980 (all from N. Atlantic) have VGP latitude $>$ -45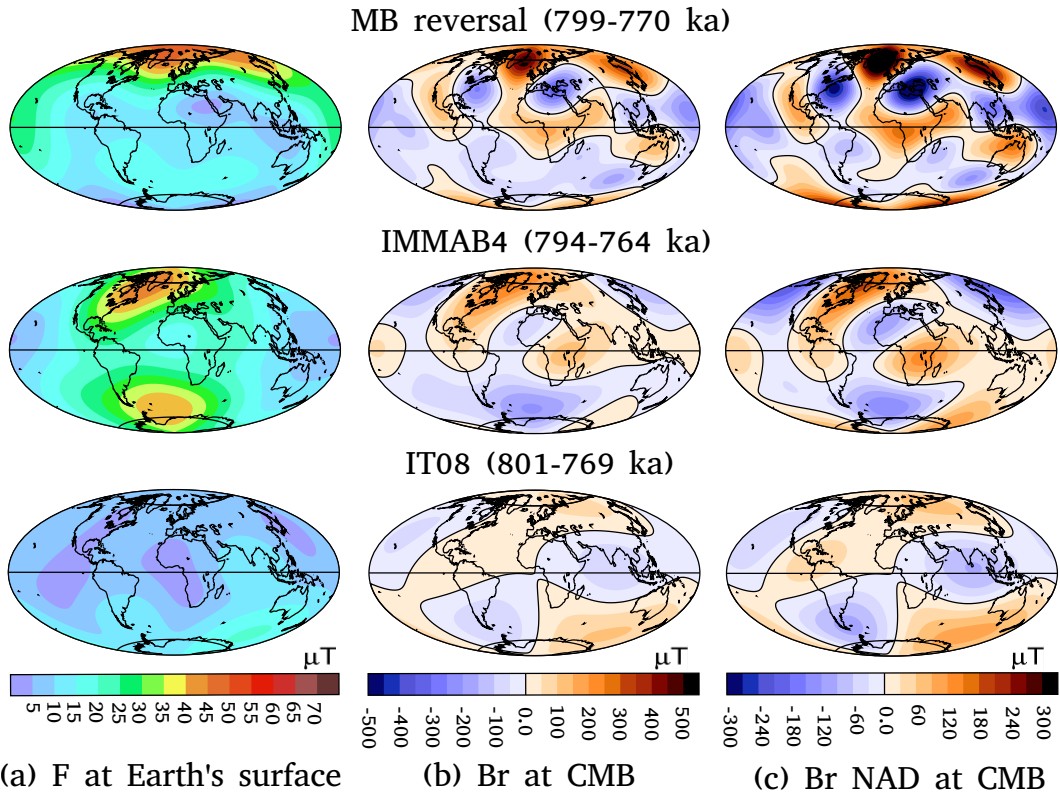°, hence of transitional polarity. The VDM of these records (Fig. S52b) are $< 4\times10^{22}$ Am^2, which is 52% of the present-day dipole moment (7.6×10^{22} Am^2), according to latest version of IGRF model (Alken et al., 2021). The transitional polarity state was confirmed in P_i curves of these records (Fig, S52d), where $P_i \geq 0.5$ (Panovska & Constable, 2017). In contrast, no transitional directions were seen in lavas across the past 890–884 ka (See Fig. S52), but lava sites from Hawaii, Tahiti, Iceland, and Antarctica have low latitude VGP latitude between 880 and 863 ka, and one Hawaiian site has VDM of 1.5×10^{22} Am^2 at 864 ka. However, if we take into account the substantial age uncertainty of these lavas sites (See Fig. S52b-d), we may deduce that these transitional directions represent Kamikatsura excursion noted in this study at 890–884 ka.
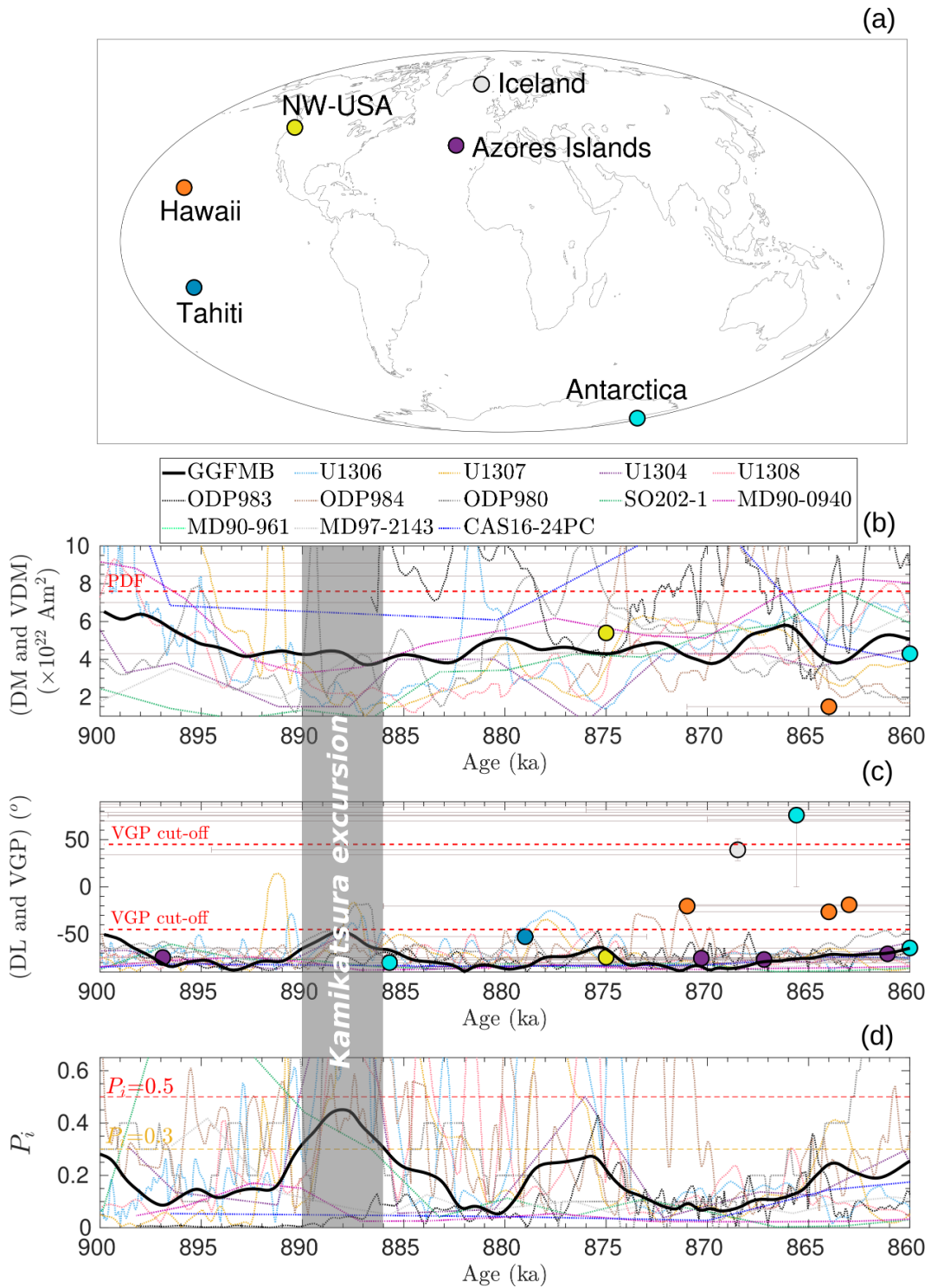
Figure S52: Investigating the Kamikatsura excursion utilizing paleomagnetic data from the GGFMB model, full-vector sediment records, and lavas, of 900–860 ka age range. (a) Geographic distribution of six lava locations (Tahiti, Hawaii, NW-USA, Iceland, Azores Islands, and Antarctica). Temporal distribution of paleomagnetic data documented from from lavas (with data and age uncertainties as grey error bars), sediment records, and GGFMB model over past 900–860 ka are plotted, in terms of: (b) dipole moment (DM) of GGFMB (thick black line) and virtual dipole moment (VDM) of individual records (colored lines); (c) model dipole latitude (DL, thick black line) and data virtual geomagnetic pole (VGP) latitudes (colored lines); and (d) paleosecular variation index (P_i) of GGFMB (thick black line) and data records (colored lines). The GGFMB model's Pi curve suggests an unstable magnetic field state with a period of ∼6 kyr, between 890 and 884 ka, as represented by grey shaded area. This is the period during which the Kamikatsura excursion likely evolved.

References

Alken, P., Thébault, E., Beggan, C. D., Amit, H., Aubert, J., Baerenzung, J., . . . others (2021). International geomagnetic reference field: the thirteenth generation. Earth, Planets and Space, 73(1), 1–25.

Ingham, M., & Turner, G. (2008). Behaviour of the geomagnetic field during the Matuyama–Brunhes polarity transition. Physics of the Earth and Planetary Interiors, 168(3-4), 163–178.

Leonhardt, R., & Fabian, K. (2007). Paleomagnetic reconstruction of the global geomagnetic field evolution during the Matuyama/Brunhes transition: Iterative Bayesian inversion and independent verification. Earth and Planetary Science Letters, 253(1-2), 172–195.

Mahgoub, A. N., Korte, M., & Panovska, S. (2023). Characteristics of the Matuyama-Brunhes magnetic field reversal based on a global data compilation. Journal of Geophysical Research: Solid Earth, e2022JB025286.

Panovska, S., & Constable, C. (2017). An activity index for geomagnetic paleosecular variation, excursions, and reversals. Geochemistry, Geophysics, Geosystems, 18(4), 1366–1375.